

California State University, San Bernardino

**CSUSB ScholarWorks**

---

Theses Digitization Project

John M. Pfau Library

---

2013

## A new phantom and gradient isocenter estimation for magnetic resonance imaging distortion correction

Zongqi Cai

Follow this and additional works at: <https://scholarworks.lib.csusb.edu/etd-project>



Part of the [Radiology Commons](#), and the [Software Engineering Commons](#)

---

### Recommended Citation

Cai, Zongqi, "A new phantom and gradient isocenter estimation for magnetic resonance imaging distortion correction" (2013). *Theses Digitization Project*. 4217.  
<https://scholarworks.lib.csusb.edu/etd-project/4217>

This Thesis is brought to you for free and open access by the John M. Pfau Library at CSUSB ScholarWorks. It has been accepted for inclusion in Theses Digitization Project by an authorized administrator of CSUSB ScholarWorks. For more information, please contact [scholarworks@csusb.edu](mailto:scholarworks@csusb.edu).

A NEW PHANTOM AND GRADIENT ISOCENTER ESTIMATION FOR MAGNETIC  
RESONANCE IMAGING DISTORTION CORRECTION

---

A Thesis  
Presented to the  
Faculty of  
California State University,  
San Bernardino

---

In Partial Fulfillment  
of the Requirements for the Degree  
Master of Science  
in  
Computer Science

---

by  
Zongqi Cai  
September 2013

A NEW PHANTOM AND GRADIENT ISOCENTER ESTIMATION FOR MAGNETIC  
RESONANCE IMAGING DISTORTION CORRECTION

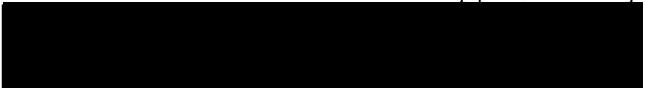
---

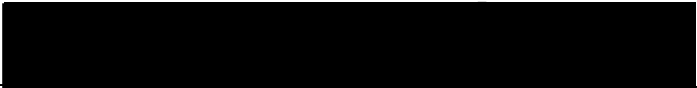
A Thesis  
Presented to the  
Faculty of  
California State University,  
San Bernardino

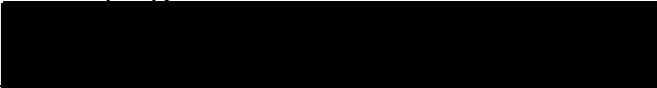
---


by  
Zongqi Cai  
September 2013

Approved by:

  
Keith Evan Schubert, Advisor, School of  
Computer Science and Engineering

  
Kay Zemojeh

  
Haiyan Qiao

  
Reinhard Schulte

*Aug 27, 2013*  
Date

© 2013 Zongqi Cai

## ABSTRACT

Magnetic Resonance Imaging (MRI) provides an excellent modality for distinguishing different tissues in the human body, which makes this modality essential for medical applications. MRI can also be used for treatment planning of medical procedures that require a great degree of geometrical accuracy such as functional radiosurgery. Unfortunately, the accuracy of MRI for medical targeting applications is compromised by the presence of geometric distortions such as non-linearities of the magnetic gradient fields or inhomogeneities of the scanner main field. Also, the correction method developed by a previous study cannot be applied due to the magnetic field inside current 3-Tesla(T) scanner is much larger than the one used in previous study.

The goal of this work was to develop and implement a numerical software-based method that can accurately correct the distortion of MR images generated by 3T MRI scanner. To accomplish this, a new phantom has been designed from scratch to capture the distortions inside 3T MRI scanner. An algorithm has been developed, based on the unique geometric feature of the new phantom, to estimate the location of gradient isocenter of the magnetic field inside 3T MRI scanner for the first time. Several other algorithms have also been developed to extract some unique features from CT and MR images of the new phantom. Using the calculated gradient isocenter and extracted data points, combining with some accurate geometric measurements of the new phantom, a set of correction parameters has been calculated. Simulated tests has shown that locations of data points corrected from MR images using the set of correction paramters are very close to their original locations. Further tests need to be performed in the

future to explore the accuracy and limitations of this distortion correction algorithm developed in this work.

## ACKNOWLEDGEMENTS

I would like to take this opportunity to thank the individuals who played a crucial role in my college education.

First and fore most, I would like to thank Dr. Schubert for giving me the oppportunity to work on the this project and tirelessly mentoring me during the time. Under his guidance, I have not only expanded my knowledge in mathematics and computer science area, I also have learned to be a better preson. Things I learned from him will be benefitial to the rest of my life.

I would also like to express my gratitude for Dr. Schulte, for patiently explaining things to me over and over again and providing funding for the crucial updates for the new phantom. The time that I have spent with Dr. Schulte has enabled me to greatly increase my knowledge in mathematics, physics, and radiation medicine.

My thanks also goes to Bob Jones who build the new phantom for us. With very limited resource avaiable to him, he has done a tremendous job in making our new phantom design become a real thing. His input has been very valuable to this project. At last, I would also like to thank to support from my family. Without them, especially my aunt, I would not have to opportunity to study in the USA, and certainly would not be able to study computer science at this point of my life.

## DEDICATION

To Mom and Dad

## TABLE OF CONTENTS

<i>Abstract</i> . . . . .	iii
<i>Acknowledgements</i> . . . . .	v
<i>List of Tables</i> . . . . .	x
<i>List of Figures</i> . . . . .	xi
 1. <i>Introduction</i> . . . . .	 1
1.1 Thesis Overview . . . . .	1
1.2 Background . . . . .	2
1.3 Significance . . . . .	5
 2. <i>Background</i> . . . . .	 6
2.1 Magnetic Resonance Imaging . . . . .	6
2.1.1 Hardware Components of an MRI Scanner . . . . .	7
2.1.2 Physics of Signal Formation and Detection . . . . .	8
2.1.3 Distortion Origin and Manifestations . . . . .	9
2.1.4 The Gradient Coils . . . . .	10
2.1.5 Physical and Mathematical Description of Nonlinear Gradient Fields . . . . .	11
 3. <i>Phantom Design</i> . . . . .	 15
3.1 Introduction . . . . .	15

3.2	Initial Design . . . . .	16
3.3	New Design . . . . .	17
3.4	Sealing NMR Tubes . . . . .	17
3.5	Updated Design . . . . .	19
3.6	Installation and Use . . . . .	19
3.7	Initial Experience . . . . .	19
3.8	Conclusion . . . . .	20
4.	<i>Gradient Isocenter Localization</i> . . . . .	21
4.1	Introduction . . . . .	21
4.2	Distortion Phantom . . . . .	22
4.3	Computational Algorithm . . . . .	23
4.4	Tube Modeling . . . . .	24
4.5	ISO-Center Coordinate Estimation . . . . .	25
4.6	Conclusion . . . . .	34
5.	<i>Data Extraction</i> . . . . .	36
5.1	Introduction . . . . .	36
5.2	Measuring Water Tanks Distances Using CT Images . . . . .	36
5.2.1	Introduction . . . . .	36
5.2.2	Canny Edges . . . . .	37
5.2.3	Surface Location . . . . .	38
5.2.4	Edge Detection On Local Surface Region . . . . .	40
5.2.5	Creating Surfaces . . . . .	43
5.3	Extracting MR Tubes Centers from MR Images . . . . .	44
5.3.1	Introduction . . . . .	44
5.3.2	Range . . . . .	45
5.3.3	Tube Centers Extraction . . . . .	47

5.4	Extracting Water Tank Edges From MR Images . . . . .	50
5.4.1	Introduction . . . . .	50
5.4.2	Algorithm . . . . .	51
6.	<i>Distortion Correction Parameters Calculation</i> . . . . .	63
6.1	Introduction . . . . .	63
6.2	XY Axis Distortion Correction Parameters Calculation . . . . .	64
6.3	Z Axis Distortion Correction Parameters Calculation . . . . .	66
7.	<i>Summary and Conclusion</i> . . . . .	67
	<i>References</i> . . . . .	68

## LIST OF TABLES

4.1	Average of 200 runs using different methods for estimating the isocenter at [4 4 3] in the presence of symmetrical distortion . . . . .	33
4.2	Average of 200 runs using different methods for estimating the isocenter at [4 4 3] in the presence of non-symmetrical distortion . . . . .	34

## LIST OF FIGURES

2.1	Simplified block diagram of a typical MRI scanner . . . . .	7
2.2	(a) Principal design of a Maxwell pair of coils generating the z-gradient field. (b) Golay arrangement of a coils producing a y-gradient. Note that the field direction coincides with the z axis. . . . .	11
3.1	Initial designs for new phantom . . . . .	16
3.2	(a) Paraffin wax at top with floatable silicon at bottom (b) Paraffin wax only (c) Machinable wax (d) Water weld (e) Silicon . . . . .	18
4.1	Phantom modeling without distortion . . . . .	24
4.2	Phantom modeling with large distortions . . . . .	26
4.3	Phantom modeling with small distortions . . . . .	26
4.4	Phantom modeling with distortion, showing differences in isocenter estimates due to how the LS equation is oriented. . . . .	31
4.5	Phantom modeling with distortion, showing how diagonal tube planes without rotation do not improve the estimates produced. . . . .	32
5.1	Sample CT image in coronal view. . . . .	37
5.2	Canny algorithm applied to coronal sequence 141 with different parameters: (a) Default parameters (b) Low threshold 0.01, high threshold 0.02 (c) Low threshold 0.02, high threshold 0.04 (d) Low threshold 0.05, high threshold 0.1 . . . . .	53

5.3	Canny algorithm applied to coronal sequence 270 with different parameters: (a) Default parameter (b) Low threshold 0.01, high threshold 0.02 (c) Low threshold 0.02, high threshold 0.04 (d) Low threshold 0.05, high threshold 0.1 . . . . .	54
5.4	Canny algorithm applied to coronal sequence 276 with different parameters: (a) Low threshold 0.02, high threshold 0.04 (b) Low threshold 0.05, high threshold 0.1 . . . . .	55
5.5	Histograms of middle column of middle slice of a coronal series: (a) mid slice intensity histogram (b) Marked overlap region (c) mid slice surface locations . . . . .	55
5.6	Histogram for boundary detection: (a) inferior tank inside edge of #270 (b) superior tank outside edge of #100 . . . . .	56
5.7	Superior outside surface artifacts: (a) Extra edge caused by tube section (b) Histogram for superior outside surface of the same image . .	56
5.8	Edge extraction intermediate results on image sequence #270's inferior tank inside edge . . . . .	57
5.9	Final edge results: (a) Edge result on image sequence #270 (b) Edge result on image sequence #100 . . . . .	57
5.10	Water tank surfaces reconstruction from CT scan, YZ view . . . . .	58
5.11	Water tank surfaces reconstruction from CT scan, XY view . . . . .	59
5.12	Noisy MR images, especially the lower tank . . . . .	60
5.13	Histogram for finding edge points . . . . .	60
5.14	gradient'histogram'state'machine . . . . .	61
5.15	MRI surface intermediate edge results: (a) Raw edge (b) after removing short edges (c) after removing large bumps (d) after removing peaks (e) final edge . . . . .	61
5.16	Lower tank lower surface result. . . . .	62

6.1	Pairing of MR tubes. (a) Pairing for X-axis (b) Pairing for Y-axis . .	65
6.2	Pairing of tank surfaces. . . . .	66

## 1. INTRODUCTION

### *1.1 Thesis Overview*

Magnetic resonance imaging (MRI) provides an excellent modality for distinguishing different tissues in the human body, which makes this modality essential for medical applications. MRI can also be used for treatment planning of medical procedures that require a great degree of geometrical accuracy such as functional radiosurgery [2]. Unfortunately, the accuracy of MRI for medical targeting applications is compromised by the presence of geometric distortions such as non-linearities of the magnetic gradient fields or inhomogeneities of the scanner main field [1, 5, 6, 7, 8, 3, 11, 12]. Gradient nonlinearities can cause over 2mm of distortion to the location of features in the image [8, 3].

The primary purpose of this thesis was to improve the distortion correction method developed in a previous thesis [4]. To do this, the following issues were addressed in this work:

- A new phantom was designed that can capture the distortion in modern 3-Tesla(T) MRI scanner.
- Algorithms were developed that can extract relevant data points from the MR images of the new phantom.

- An new algorithm was developed that can accurately estimate the gradient isocenter of the magnetic field inside 3T MRI scanners.
- An algorithm was developed that can determine the correction parameters, which can then be used to generate corrected MR images.

The thesis is organized as follows. After the introduction, Chapter 2 gives background information on MRI, it's geometric distortion, and approaches to corrected. Chapter 3 describe the design details of the new phantom and several phases and changes the design went through. The main feature of the final design of the phantom and their importance will be discussed. The next chapter discusses the algorithm for estimation of gradient isocenter based on new phantom design. Chapter 5 describe a series of algorithms used to extract relevant data from MR and CT images. CT images were used in this work to obtain accurate dimensions inside the phantom. Chapter 6 describes the procedure to estimate the parameters of the model that corrects the distorted MR images. The final chapter summarizes the main results and suggests future work.

## 1.2 Background

The research project associated with this thesis relates to the correction of MRI images that will be used for functional proton radiosurgery at Loma Linda University Medical Center (LLUMC). The clinical application of protons was first suggested over 60 years ago [13]. The ability to penetrate human tissue, delivering high dosage of proton beams at a target region and being able to concentrate on a very small target area make protons ideal for use in noninvasive surgery [13]. Currently, Loma Linda

University Medical Center (LLUMC) is using proton beams to treat patients with tumors or vascular malformations in the brain.

Due to the effectiveness of proton radiosurgery, a new system is proposed that targets functional disorders in the brain, such as trigeminal neuralgia and Parkinson's disease by creating small lesions in the brain regions affected by the disease. The current system can treat targets as small as 1 to 3 cm. Target localization is accomplished using CT and projection angiography. MRI will to be used for target localization in the new system. The major obstacle of using MRI is the geometric distortion on MRI images caused by the nonlinearity of the magnetic gradient fields of the scanner.

For the proposed application, two of the most important requirements for a successful distortion correction are:

1. The distortion correction must have submillimeter accuracy.
2. The correction process must be finished within 15 minutes.

This work is based on a published method for gradient nonlinearity correction using a cubic phantom MRI data set [3], which was also subject of a previous thesis by Tom S. Lee [4]. The published method utilizes the sum of spherical harmonics to model the geometrically warped planes of the cube, and applies the model to correct arbitrary image sets acquired with the same scanner. The cube is placed in the MRI scanner such that the cube's center is exactly in the center of the MRI scanner. This work assumes the center of the MRI scanner corresponds to the isocenter of the magnetic field of the scanner. Opposite faces of the phantom are averaged, and three midplanes are fit to these surfaces. Due to the symmetric property of the magnetic field, the

midplanes of different orientations of the phantom cube are corrected. Through each midplane, the ideal planes of different surfaces of the cube are calculated simply by shifting the midplane to the direction of the ideal plane by one-half the length of the cube. For each pixel on the ideal plane, the sum of spherical harmonics equation 6.1 is applied to transform that pixel to the corresponding location on the distorted plane.

$$\bar{\alpha} = \alpha(1 + K_{\alpha_0}(x^2 + y^2) + K_{\alpha_1}z^2 + K_{\alpha_2}z^2(x^2 + y^2) + K_{\alpha_3}(x^2 + y^2)^2 + K_{\alpha_4}z^4) \quad (1.1)$$

Where  $\bar{\alpha}$  and  $\alpha$  are corrected and distorted 3D coordinate respectively;  $x$ ,  $y$  and  $z$  are coordinates of  $\alpha$  on each axis;  $K_{\alpha_i}$  are distortion parameters. Thus the distortion parameters in equation 6.1 are computed using linear least squares technique.

Several assumptions are made for this model:

- The phantom is (reasonably) centered with respect to the gradient isocenter of the scanner.
- The distortion is (reasonably) symmetric for each pair of faces.
- The origin of the DICOM patient coordinate system coincides with the position of the gradient isocenter.

In reality, however, these assumptions are not valid. Due to the geometry of the MR scanner, the phantom cannot be centered, and the phantom center will always be located in the upper half of the circular scanning plane. The issue of phantom centering has been identified as a crucial factor in the quality of distortion correction.

Improper centering of the phantom in the scanner produces strong asymmetry in the phantom surfaces, thereby violating the assumption of symmetry of the distortion.

The assumption that the origin of the DICOM patient coordinate system corresponds to the isocenter of the magnetic field in the MRI scanner is also invalid. Siemens engineers have confirmed that the exact location of the gradient isocenter is unknown. Thus, the assumption that the origin of the DICOM patient is at the same location as the gradient isocenter will further compromise the accuracy of the distortion correction method.

In addition, with the introduction of the new 3T MR scanner with a larger bore, the previous phantom, which was designed for a 1.5 T scanner with a much smaller bore, turned out to be inadequate. The new scanner had only minimal distortion in the area probed by the original phantom with 16 cm diameter. A larger phantom was clearly needed that also better probed the circular field of view of the scanner.

### *1.3 Significance*

Geometric distortions are critical for the use of MRI in accurate medical targeting. Procedures such as functional proton radiosurgery that deliver very high doses to small targets very accurate targeting is an absolute requirement. The built-in distortion correction of modern MRI scanners is probably not accurate enough for such procedures, and distortion correction methods that are based on measurements of the nonlinearity in the actual scanner are needed. With the work accomplished in this thesis, we have come a step closer to using MRI for such procedures. The phantom and algorithms developed will also be useful for other MRI targeting procedures.

## 2. BACKGROUND

### 2.1 *Magnetic Resonance Imaging*

The image in MRI is a multidimensional data array representing the spatial distribution of nuclear magnetic properties of the image object, although the original data acquired represents the frequency distribution of the responses of a multitude of hydrogen nuclei in an inhomogeneous magnetic field. The information is usually organized as 2D images, presented discretely in form of image pixels such that each pixel is a 2D representation of the measured physical quantity in the corresponding object voxel (a small 3D box).

The value of MR image pixels (or corresponding voxels) depends on many intrinsic physical parameters, including the nuclear spin density,  $\rho$ , the spin-lattice relaxation time  $T_1$ , the spin-spin relaxation time  $T_2$ , molecular motions (diffusion and perfusion), susceptibility effects, chemical shift differences, etc. The relative weight of these parameters in their contribution to the image contrast can be influenced by operator-selectable parameters, such as the repetition time  $TR$ , echo time  $TE$ , and flip angle  $\alpha$ . However, this will not be further discussed here because it is not necessary for correcting the origin of gradient nonlinearity.

### 2.1.1 Hardware Components of an MRI Scanner

The main components of the MRI scanner system are shown in Fig 2.1. It consists of three main hardware components: the main magnet (blue), the gradient coil system (red), and the radiofrequency (RF) coil system (green). The main magnet can be thought of as a large tube, which fits inside the bore of the MR scanner. The housing of the three gradient coils also takes the form of a tube, which fit inside the main magnet. The RF coil, which both produces and receives RF signals, takes the shape of another tube that fits inside the gradient coils. Hence the space in which the body part to be imaged is placed is a cylindrical volume with the longitudinal axis (z) being parallel to the patient longitudinal body axis and the diameter matching the inner diameter of the coil housing. If the head is imaged, a removable RF head coil, which has a better signal to noise ratio than the body coil, is placed inside the body coil.

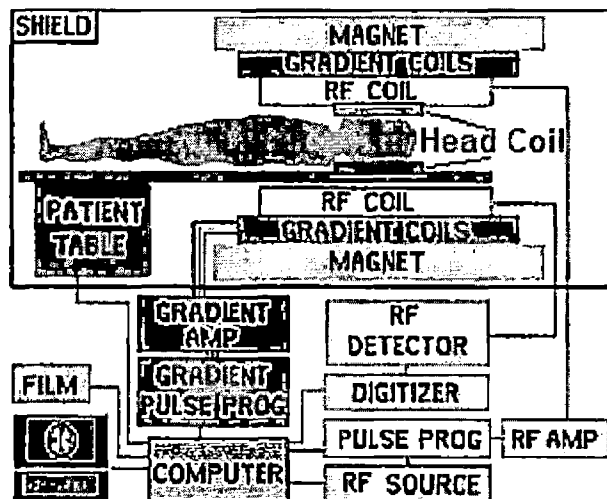


Fig. 2.1: Simplified block diagram of a typical MRI scanner

### 2.1.2 *Physics of Signal Formation and Detection*

The signal source in MRI is the macroscopic magnetization produced by excited nuclear spins in the imaged object. Spin is a fundamental quantum property of elementary particles just like electrical charge or mass, which is related to the angular momentum of the nucleus. In classical terms, angular momentum is due to spinning of an object about its axis. Spin quantum numbers come discrete, i.e., in multiples of  $\frac{1}{2}$ , and can be either positive or negative. The total spin quantum number of  $\frac{1}{2}$  paired protons and neutrons equals zero, while unpaired protons and neutrons in a nucleus each contribute a spin quantum number of  $\frac{1}{2}$ . Thus, a nucleus with an uneven number of nucleons (protons or neutrons) has a nonzero spin quantum number, which is a multiple of  $\frac{1}{2}$ , and a large number of them can, therefore, produce a net magnetization when placed in an external magnetic field. The most abundant nucleus with uneven number of nucleons in the human body is hydrogen with just one proton.

In MRI, an ensemble of nuclei of the same type, such as hydrogen, present in an object being imaged is called a nuclear spin system. Although nuclear spin is a property of the individual nucleus, characterized by quantum mechanics, with the large number of nuclei present in bulk matter, the bulk behavior of a spin system can be described in classical physics terms and the macroscopic magnetization is no longer discrete.

A single nucleus with a nonzero spin, such as hydrogen, creates a small magnetic field, which is represented by the vector quantity  $\mu$ , called the nuclear magnetic moment. Spin angular momentum  $\mathbf{J}$  and magnetic moment are linearly related to each other by

$$\mu = \frac{\gamma}{2} \pi J \quad (2.1)$$

which  $\gamma$  is gyromagnetic ratio.

### 2.1.3 Distortion Origin and Manifestations

Spatial indexing in MRI is accomplished by gradient coils in three orthogonal directions. In image reconstruction, gradients are assumed linear throughout the imaging volume. Due to pragmatic constraints, further considered below, it is difficult to achieve this situation.

For a patient to fit comfortably, the bore of the main magnet must be as large as possible. The larger the bore, the more difficult it is to generate a linear gradient. In general, the gradient along the axis of the main magnet (z axis) has the highest linearity compared to the other two directions (x and y) due to physical constraints.

Consider a slice of constant z, read in x direction. In the slice image, gradient field non-linearity distortion manifests itself in two ways. First, due to non-linearities in the x gradient,  $G_x$ , and in the y-gradient,  $G_y$ , there is a systematic transverse distortion in the slice plane. Second, because of the gradient field non-linearity, a potato chip effect takes place along the slice selection direction (z). Although MRI slices are usually considered to be planes, in actuality, because of gradient field non-linearity, these planes tend to warp into a potato chip-like shapes. This distortion is difficult to correct in 2D imaging but can be, in principle, corrected in 3D imaging methods.

#### 2.1.4 The Gradient Coils

Misregistration caused by gradient field non-linearities occur in all three directions. The magnetic fields generated by the three gradient coils and the main magnet lie along the  $z$ -axis. Due to the strength of the main  $B_0$  field, any other component of the gradient fields can be neglected.

The  $z$ -gradient coil is designed to produce a linear variation in the  $z$ -component of the field along the axis of the magnet, with a high degree of gradient uniformity in the transverse plane. Circular wire loops are the most obvious choice since they are azimuthally symmetric and possess reasonable radial uniformity. Since the gradient fields have to be symmetric with respect to the gradient isocenter, the coils are usually arranged as pairs. For the  $z$ -gradient, the current in the coil pair, called Maxwell pair, is equal in magnitude, but opposite in direction (see Fig. 2.2 (a)). Coils on one side of the  $z = 0$  plane generate fields parallel to  $B_0$  while fields due coils on the other side are anti-parallel to  $B_0$  leading to an overall field variation along  $z$ . The relation between the radius  $a$  of the coils and their axial distance  $d$  is optimized in order to minimize all but the linear  $z$ -term in the polynomial expansion of the field described below.

The design of the gradient coils in  $x$  and  $y$ -direction is more complicated. The principle design, called Golay arrangement, is shown in Fig. 2.2(b). The  $x$ - and  $y$ -gradient coils are identical except for a rotation by 90 degrees.

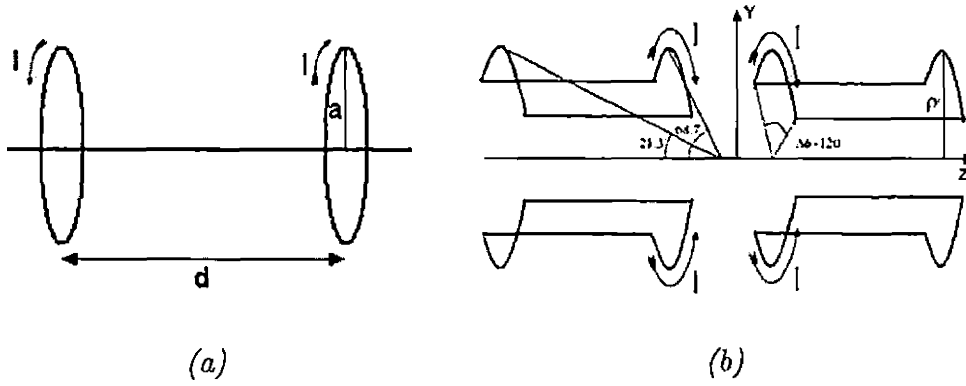


Fig. 2.2: (a) Principal design of a Maxwell pair of coils generating the z-gradient field. (b) Golay arrangement of a coils producing a y-gradient. Note that the field direction coincides with the z axis.

### 2.1.5 Physical and Mathematical Description of Nonlinear Gradient Fields

The following description of nonlinear gradient field was given by Dr. Sumanaweera in his thesis [10]. Let  $\mathbf{B}$  the magnetic flux density and  $\mathbf{H}$  be the magnetic field intensity vectors produced by any of the gradient coils. The relationship between these vector quantities is

$$\mathbf{B} = \mu \mathbf{H} \quad (2.2)$$

where  $\mu$  is the permeability of the medium. Gradient fields are usually quasistatic (slowly varying in time) magnetic fields, therefore, displacement currents in the medium inside the coil may be ignored unless very rapid sequences are used. Electromagnetic field theory tells us that a quasistatic magnetic field in a current free region can be described by a scalar magnetic field potential such that

$$\mathbf{H} = -\nabla \psi \quad (2.3)$$

A fundamental property of magnetic fields is that its divergence is always zero, thus

$\nabla \cdot \mathbf{B} = 0$  everywhere, and therefore the scalar magnetic potential satisfies Laplaces equation:

$$\nabla^2 \psi = 0 \quad (2.4)$$

It can be shown that solutions of Laplaces equation can be expressed as linear combinations of homogeneous polynomials in the coordinates  $x, y, z$ . In order to describe the nonlinearity of a gradient field, one usually decomposes the field into the ideal linear term and additional nonlinear field terms; the latter are expanded into homogenous polynomials. Furthermore, if one assumes circular symmetry, which means that there is no specific angular dependence of the nonlinear field terms, one obtains following general expressions for the three gradient fields  $B_x, B_y$ , and  $B_z$

$$\begin{aligned} B_x &= G_x x \left[ 1 + \sum_{i=1}^{\infty} A_i \sum_{j=0}^i a_j z^{2(i-j)} (x^2 + y^2)^j \right] \\ B_y &= G_y y \left[ 1 + \sum_{i=1}^{\infty} B_i \sum_{j=0}^i b_j z^{2(i-j)} (x^2 + y^2)^j \right] \\ B_z &= G_z z \left[ 1 + \sum_{i=1}^{\infty} C_i \sum_{j=0}^i c_j z^{2(i-j)} (x^2 + y^2)^j \right] \end{aligned} \quad (2.5)$$

Note that if the nonlinear terms vanish, the gradient fields become perfectly linear. In general, the higher order polynomials in these field equations are insignificant (contribute very little to the field) and can therefore be ignored. In practice, it is sufficient to include only polynomials up to the second order  $i = 2$  in  $x^2, y^2$ , and  $z^2$ . Thus, the field gradient expressions become:

$$\begin{aligned}
B_x &\cong G_x x \left[ 1 + K_{x0}(x^2 + y^2) + K_{x1}z^2 + K_{x2}z^2(x^2 + y^2) + \right. \\
&\quad \left. K_{x3}(x^2 + y^2)^2 + K_{x4}z^4 \right] \\
B_y &\cong G_y y \left[ 1 + K_{y0}(x^2 + y^2) + K_{y1}z^2 + K_{y2}z^2(x^2 + y^2) + \right. \\
&\quad \left. K_{y3}(x^2 + y^2)^2 + K_{y4}z^4 \right] \\
B_z &\cong G_z z \left[ 1 + K_{z0}(x^2 + y^2) + K_{z1}z^2 + K_{z2}z^2(x^2 + y^2) + \right. \\
&\quad \left. K_{z3}(x^2 + y^2)^2 + K_{z4}z^4 \right]
\end{aligned} \tag{2.6}$$

where we have introduced new constants  $K$  (for example,  $K_{x0} = A_0 a_0$ ). Since the coordinate distortion function can be expressed as:

$$x' = x(1 + \nabla G_x) \equiv f_x(x) \tag{2.7}$$

we have:

$$\begin{aligned}
f(x) &= x \left[ 1 + K_{x0}(x^2 + y^2) + K_{x1}z^2 + K_{x2}z^2(x^2 + y^2) + \right. \\
&\quad \left. K_{x3}(x^2 + y^2)^2 + K_{x4}z^4 \right] \\
f(y) &= G_y y \left[ 1 + K_{y0}(x^2 + y^2) + K_{y1}z^2 + K_{y2}z^2(x^2 + y^2) + \right. \\
&\quad \left. K_{y3}(x^2 + y^2)^2 + K_{y4}z^4 \right] \\
f(z) &= G_z z \left[ 1 + K_{z0}(x^2 + y^2) + K_{z1}z^2 + K_{z2}z^2(x^2 + y^2) + \right. \\
&\quad \left. K_{z3}(x^2 + y^2)^2 + K_{z4}z^4 \right]
\end{aligned} \tag{2.8}$$

Equation 2.8 can be conveniently written in matrix form as

$$r' = r + K \cdot F(r) \tag{2.9}$$

where  $r'$  is the distorted coordinate vector derived from the undistorted vector  $r$ ,  $K$  is the distortion parameter matrix formed by the elements  $K_{\alpha i}$ ,  $\alpha = x, y, z, i = 0, 1, \dots, 4$ , and  $F(r)$  is a nonlinear six-dimensional vector field given by

$$F(r) = \begin{bmatrix} x(x^2 + y^2) \\ xz^2 \\ xz^2(x^2 + y^2) \\ x(x^2 + y^2)^2 \\ z^4 \end{bmatrix} \quad (2.10)$$

### 3. PHANTOM DESIGN

#### 3.1 *Introduction*

Magnetic Resonance Imaging (MRI) provides an excellent modality for distinguishing different tissues in the human body, which is essential for medical applications. When MRI is used for stereotactic treatment planning, its geometric accuracy is crucial. Previous studies have been conducted to correct the distortion caused by nonlinearity of the MRI scanners magnetic gradient fields by imaging a cubic phantom [3], [8] and defining distortion correction functions based on the distorted appearance its surfaces. Correct mathematical handling of the distortion correction function required that the cube was centered about the magnetic isocenter, which is defined as the common center of the three magnetic gradient fields and is not very accurately known. New 3-Tesla MRI systems have a larger bore, making the previous phantom design impractically small for probing the field nonlinearity in the periphery of the bore, as the phantom cannot be scaled up due to constraints related to weight and cost of manufacturing. We are introducing a new phantom design using a different approach, which can be built to a larger size, improves accuracy of distortion characterization, and reduces cost.

### 3.2 Initial Design

The original phantom design, a 16-cm oil-filled cube, could not be scaled up due to weight and manufacturing constraints. Our first modification was to look at changing the material to FR-4 since it is rigid, very flat, and could be submerged for short periods of time to permit scanning the solid liquid interface in an MRI machine. Since most of the distortion is visible only in the corners, this was rapidly replaced by 8 corners of a virtual cube, which could be connected by a rigid frame. The weight of a tank to submerge either of these designs to allow scanning was prohibitive, requiring a complete redesign.

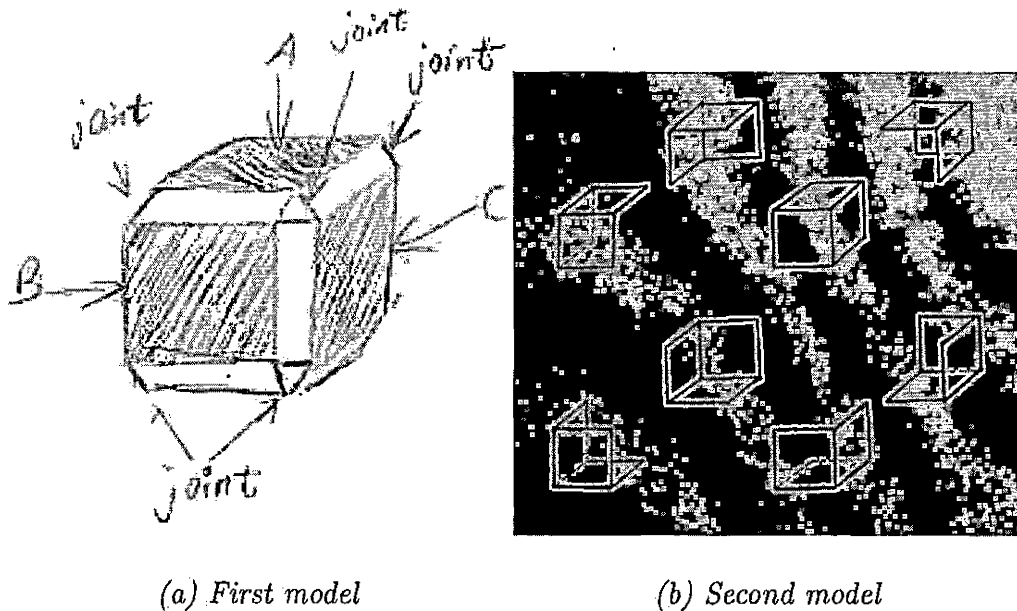


Fig. 3.1: Initial designs for new phantom

### 3.3 *New Design*

The phantom is shaped to be as large as possible, while still fitting in the head coil of the scanner, so as to achieve the maximum quality of signal and largest distortion. The phantom is an octagonal prism with 205 mm between opposite sides. Each face of the octagonal prism is composed of 8 high precision NMR tubes that are 5mm in outer diameter and 205 mm in length. These tubes are filled with copper sulfate solution to generate a strong signal in an MRI scanner. The tubes are placed parallel to the magnetic field so they will cause less susceptibility distortion [9], and thus provide more accurate information on the gradient field. In the center of the phantom is a large water tank to help intensify the signals generated by the tubes. At one end of the phantom is a cylindrical tank filled with copper sulfate, with a number of small solid cylinders in a hexagonal pattern that are connecting the two surfaces of the tank. These cylinders are used to maintain the long-term accuracy of the two surfaces, making sure they won't deform, and are also aligned to the field to minimize their effect on the field. The data generated from 64 tubes mounted on the sides are designed to give us x and y axis distortion information, and the end tank is designed to provide z-axis distortion data, allowing a complete 3-D distortion correction with a relatively small amount of data.

### 3.4 *Sealing NMR Tubes*

Our original idea for sealing the NMR tubes was to use paraffin wax, either with or without a silicon seal. Paraffin was heated and a liquid drop was then added to the tube as a seal, but had an uneven bottom caused by the rapid solidifying of

the wax, when it came in contact with the copper sulfate. Additionally, it tended to trap air bubbles, which made the end very hard to work with in the images. Worst yet, after a few weeks the liquid level in the tubes started to drop. We decided to compare three potential alternatives: machinable wax, water weld, and silicon sealer. As the images on the right show, the silicon was far and away the best. There was no leakage lost, and since the setup time was slower on the liquid side it ended up being almost completely flat. Every feature was met, and it was also the most cost effective solution.

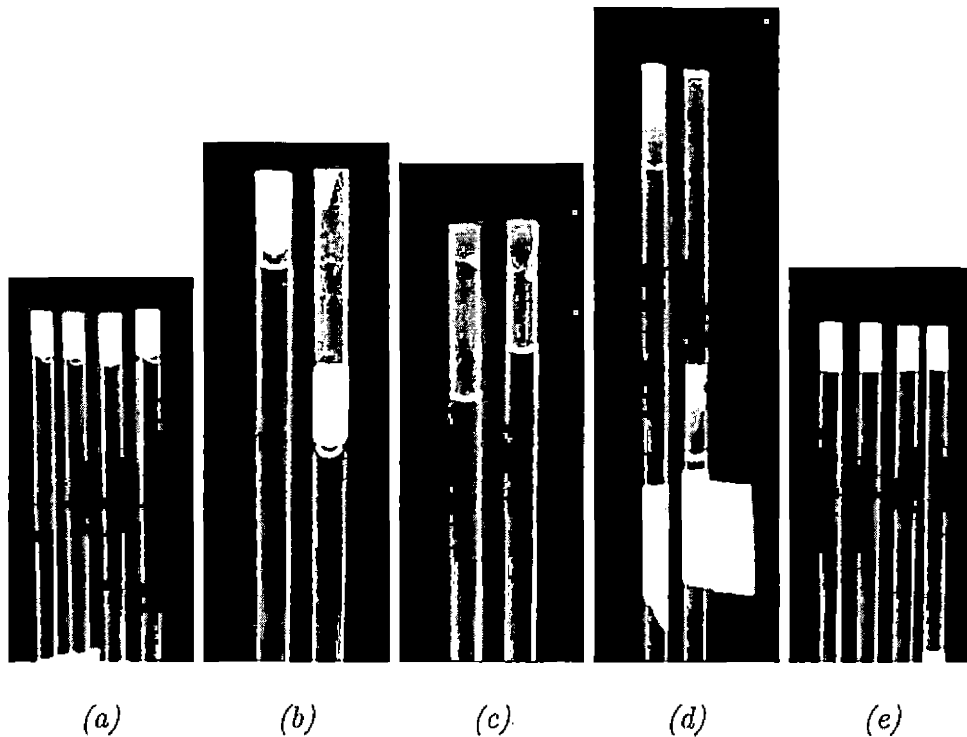


Fig. 3.2: (a) Paraffin wax at top with floatable silicon at bottom (b) Paraffin wax only (c) Machinable wax (d) Water weld (e) Silicon

### *3.5 Updated Design*

### *3.6 Installation and Use*

The new phantom is designed to rest in the head coil of a 3T MRI scanner. It has a back plate with several leveling screws to align the phantom in the head coil using the laser alignment system. This alignment is aided by alignment marks on the outside of the phantom. The phantom is then moved into the MRI scanner, and its center is placed as close to the isocenter as possible. While it is not required to be centered, centering does improve the performance. A quick alignment scan is used to ensure the phantom is in the best location possible. When this is done the scan is taken and processed using distortion detection and correction software, which is not subject of the present presentation.

### *3.7 Initial Experience*

The original phantom design, a 16-cm oil-filled cube, could not be scaled up due to weight and manufacturing constraints. Our first modification was to look at changing the material to FR-4 since it is rigid, very flat, and could be submerged for short periods of time to permit scanning the solid liquid interface in an MRI machine. Since most of the distortion is visible only in the corners, this was rapidly replaced by 8 corners of a virtual cube, which could be connected by a rigid frame. The weight of a tank to submerge either of these designs to allow scanning was prohibitive, requiring a complete redesign.

### 3.8 Conclusion

A new phantom for the measurement and correction of nonlinear gradient field distortion of MRI systems is presented. It is lighter, more economic, and allows for both more accurate measurement of field distortion and the location of the isocenter.

## 4. GRADIENT ISOCENTER LOCALIZATION

### 4.1 *Introduction*

Magnetic resonance imaging (MRI) provides an excellent modality for distinguishing different tissues in the human body, which makes this modality essential for medical applications. MRI can also be used for treatment planning of medical procedures that require a great degree of geometrical accuracy such as functional radiosurgery [2]. Unfortunately, the accuracy of MRI for medical targeting applications is compromised by the presence of geometric distortions such as non-linearities of the magnetic gradient fields or inhomogeneities of the scanner main field [1, 5, 6, 7, 8, 3, 11, 12]. Gradient nonlinearities can cause over 2mm of distortion to the location of features in the image [8, 3].

Modern MRI scanners have built-in distortion correction algorithms, that rely on knowledge of the magnetic field configuration and its distortion. Built-in algorithms, which are usually proprietary, are designed based on assumed knowledge of the geometry and location of the gradient coils. A more practical approach is to use a phantom of known geometry and to derive the distortion by analyzing the MRI images generated with such a phantom [1, 5, 6, 7, 8, 3, 11, 12]. This method has the advantage that a scanner-specific correction can be applied, which can also take into account potential changes in the gradient fields over time.

Accurate knowledge of the gradient isocenter is essential to very accurate distortion correction methods. To our knowledge, existing distortion correction algorithms, both built-in and phantom based, make the assumption that the gradient isocenter coincides with the origin of the DICOM coordinates. This assumption may not be accurate and should not be used if a high degree of accuracy is necessary.

The goal of this work was to develop and implement a numerical software-based method to estimate the gradient isocenter of the magnetic field inside an MRI scanner using the MRI scan of a custom-built phantom. In our previous work [5, 6, 7, 8], we used an oil filled plexiglass cube with  $159.50\text{mm} \times 159.70\text{mm} \times 158.11\text{mm}$  dimension that was designed to fit MR scanners that were available at that time. Current MRI scanners have a significantly wider aperture, which necessitates a larger phantom to characterize the field distortion. Furthermore, since the lower part of the scanner aperture is occupied by the scanner table, the scanning area occupied by the phantom or the patient is not centered on the gradient isocenter, making correction methods that assume that the phantom is centered with respect to the gradient isocenter [5, 6, 7, 8, 3] obsolete and potentially inaccurate.

## 4.2 *Distortion Phantom*

A new phantom design was developed with the intention to probe the distortion in the 50 cm field-of-view (FOV) of a modern 3T MRI scanner (Magnetom Trio, Siemens). Due to the geometry of the gradient field nonlinearity, the distortion is largest in the outer fringes of the FOV [5, 6, 7, 8]. Capturing distortion data in the periphery of the FOV is important for better accuracy of the distortion correction. Building

a very large cubical oil-filled phantom is a challenge due to weight limitations and limited capability to accurately machine a very large flat surface. Thus it was felt to be impractical to simply scale up the original phantom. Another limitation is that the phantom needs to fit inside the scanner head coil which needs to be used to achieve a sufficiently high signal-to-noise ratio. To meet all requirements, we designed a phantom that is comprised of 64 NMR glass tubes of 3 mm inner diameter, filled with copper sulfate and arranged in 8 surfaces forming an octagon. A water-filled cylinder in the middle of the octagon ensures a good signal generated by the tubes. The distance between tubes on the opposite side of the surface is 205mm, which is about 28% wider than the original phantom. In addition we also added four more surfaces to provide data and better fit the headcoil. There are 8 removable tubes on each surface with 10 mm gap between adjacent tubes. Each tube is about 207 mm long, which is also an increase of about 28% in length from the original phantom. Tubes are placed along the main axis of the magnetic  $B_0$  field to reduce the effects of chemical shift and magnetic susceptibility and resulting in high-quality axial images.

### 4.3 Computational Algorithm

The algorithm we described here is using simulated data set that is based the geometric property of the phantom and the properties of the MR images. The MR images we are using have 1mm per pixel resolution for every image and 1mm thickness between two adjacent planes. In the simulation, we will be using millimeters as unit for each data point. Since the images we are using to collect data points are all axial scans, we will only add noise to x and y coordinate of each data point.

#### 4.4 Tube Modeling

The tubes are 203 mm long. So our simulation data is ranging from -100 to 100 on  $z$  axis for each tube. The arrangement of the tubes could be seen in Figure 4.1. Our algorithm is based on two standard assumptions [5, 6, 7, 8, 3].: (1) the distortion in MR images are only caused by the magnetic field inside MRI scanner and (2) the magnetic field can be perfectly described using the sum of spherical harmonic.

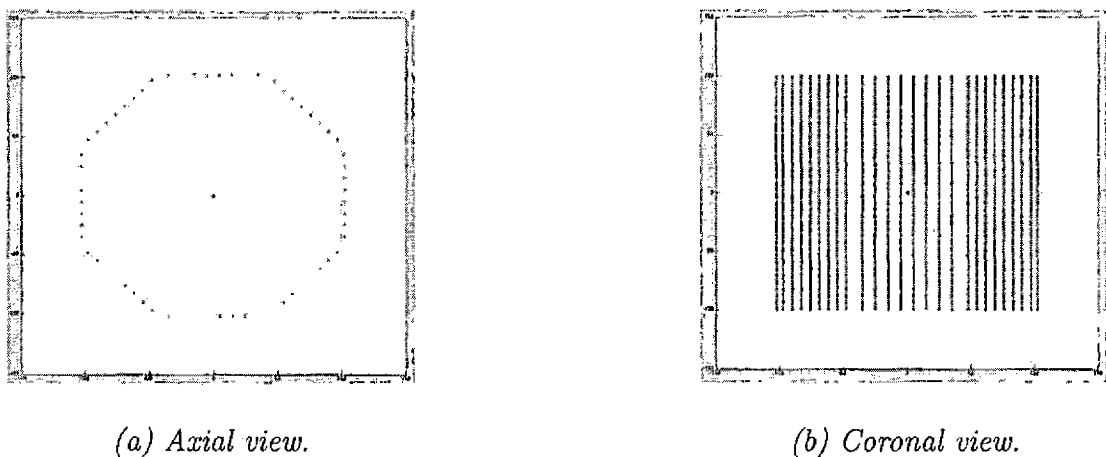


Fig. 4.1: Phantom modeling without distortion

The spacial coordinate of the phantom must be transformed into a coordinate relative to the gradient isocenter of the magnetic field, see Equation 4.1, then using the first 5 terms of the spherical harmonic we can estimate a offset in  $x$ ,  $y$ ,  $z$  direction, see Equation 4.4. Finally this offset is added the original coordinate to create a distorted model, see Equation 4.5. Also a very key requirement for this algorithm is that the  $z$ -axis the phantom which is parallel to the tubes must be aligned with the  $z$ -axis of the magnetic field.

$$\begin{bmatrix} x' \\ y' \\ z' \end{bmatrix} = \begin{bmatrix} x \\ y \\ z \end{bmatrix} - \begin{bmatrix} x_{iso} \\ y_{iso} \\ z_{iso} \end{bmatrix} \quad (4.1)$$

$$K = \begin{bmatrix} K_{x_0} & K_{x_1} & K_{x_2} & K_{x_3} & K_{x_4} \\ K_{y_0} & K_{y_1} & K_{y_2} & K_{y_3} & K_{y_4} \\ K_{z_0} & K_{z_1} & K_{z_2} & K_{z_3} & K_{z_4} \end{bmatrix} \quad (4.2)$$

$$\begin{bmatrix} \alpha \\ \beta \\ \zeta \end{bmatrix} = K \begin{bmatrix} x'^2 + y'^2 \\ z'^2 \\ z'^2(x'^2 + y'^2)^2 \\ (x'^2 + y'^2)^2 \\ z'^4 \end{bmatrix} \quad (4.3)$$

$$\begin{bmatrix} \Delta x \\ \Delta y \\ \Delta z \end{bmatrix} = \begin{bmatrix} x' \alpha \\ y' \beta \\ z' \zeta \end{bmatrix} \quad (4.4)$$

$$\begin{bmatrix} \bar{x} \\ \bar{y} \\ \bar{z} \end{bmatrix} = \begin{bmatrix} x + \Delta x \\ y + \Delta y \\ z + \Delta z \end{bmatrix} \quad (4.5)$$

#### 4.5 ISO-Center Coordinate Estimation

Using a exaggerated distortion parameter we can visualize the shape of the distortion model. Without distortion, the phantom appears as in Figure 4.1. With large distortions, the phantom appears as in Figure 4.2, which is useful to understand the

form of the distortions. A more realistic distortion can be seen in Figure 4.3, which uses distortion parameters from [8].

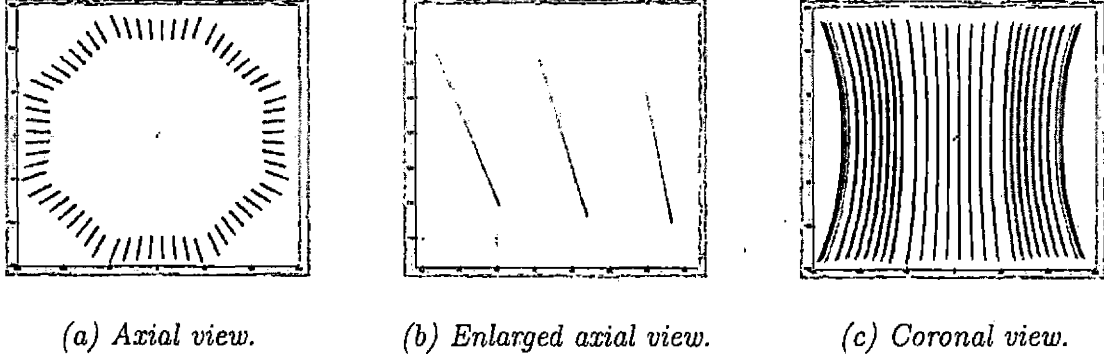


Fig. 4.2: Phantom modeling with large distortions

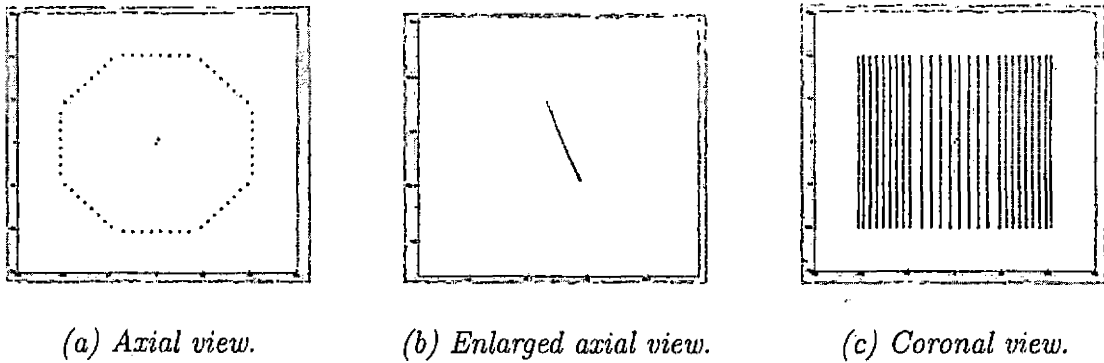


Fig. 4.3: Phantom modeling with small distortions

Distortion in the sum of spherical harmonics is coupled in the  $x$  and  $y$  directions (orthogonal to axis), making the  $z$  axis independent. Noise and distortion are thus very different in the  $z$  direction as opposed to the  $x$ - $y$  plane. We break down the gradient isocenter coordinate estimation into two big steps: estimation of  $z$  coordinate and estimation of  $x, y$  coordinate.

### *Z-Coordinate Estimation*

Since the distortion model is based on sum of spherical harmonics, the shape of the distorted data for each tube is an even polynomial function. Figure 4.3 shows that the realistic distortion is quite small, being about a maximum of 2 pixels, and the smaller the distortion the more sensitive the problem becomes. With the first four terms of sum of spherical harmonics, the shape of the each tube can be seen as part of a polynomial function of 4th degree. Since the data points of tubes only represent the middle section of the 4th degree polynomial function, it is also very similar to a shape of quadratic function. The offset between the largest distortion and the smallest distortion can be as small as 1mm. With such a small margin, it is more practical to fit the data points to simpler model than a 4th degree polynomial. Only the first spherical harmonic is needed in order to estimate the point where gradient is zero to measure the isocenter. Furthermore, the first term of the sum of spherical harmonics has the largest signal to noise ratio, so we use a quadratic model to fit the data points.

We can see the distorted tube models' middle part is bending toward the center with both end bending outward. If we were to fit each tubes to a parabola and locate the point where its gradient is zero, that point's z-coordinate should be the same as the z-coordinate of the gradient isocenter of the magnetic field. The z-coordinate is measured for all 64 tubes and the result averaged. The resulting estimation is within 0.1 mm of the actual z-coordinate.

### *X,Y Coordinate Estimation*

The estimation of the x and y coordinates of the isocenter is the more difficult problem. We are assuming that the difference between the distortion on x and y direction are so small that we can treat them as if they are the same. When this is not true, the errors on the isocenter location will be asymmetric, and it will be even more important to maintain a good numerical method to estimate the isocenter. With that in mind, the distorted data of a tube should all stay on a plane which isocenter is also in. The intersection of such planes from each tube should be a line that goes through isocenter. Using the isocenter estimated from previous step we should obtain an estimation of x and y coordinate.

Since the tubes were aligned to the z-axis to reduce magnetic field distortion by the tubes, the range of data in the z-direction is of necessity larger. In the x-y plane the range of points is controlled by the distortion, and is thus only a few pixels. The resulting equations are highly sensitive, requiring careful handling in our numerical algorithm.

The equation of a plane in three dimensions is as follows.

$$ax + by + cz + d = 0 \tag{4.6}$$

Rewriting eq 5.2 with the measured data, we can solve for the plane each tube lies in. This in turn can be used to find the intersection of the planes, which is the

isocenter.

$$\begin{aligned}
 -\frac{b}{a}y - \frac{c}{a}z - \frac{d}{a} &= x & (4.7) \\
 \begin{bmatrix} y_0 & z_0 & 1 \\ \vdots & \vdots & \vdots \\ y_n & z_n & 1 \end{bmatrix} \begin{bmatrix} -b/a \\ -c/a \\ -d/a \end{bmatrix} &= \begin{bmatrix} x_0 \\ \vdots \\ x_n \end{bmatrix} \\
 -m_x &= \frac{b}{a} \\
 k_x &= -\frac{c}{a}z_{iso} - \frac{d}{a} \\
 x &= -m_x y + k_x \\
 \begin{bmatrix} 1 & m_x \end{bmatrix} \begin{bmatrix} x \\ y \end{bmatrix} &= k_x & (4.8)
 \end{aligned}$$

Note that eq 5.2 can be rewritten so either x or y is independent, which affects the error in standard least squares. This becomes particularly important when the non-linearity is not the same in the x and y directions, as scaling is also well known

to cause problems for least squares.

$$-\frac{a}{b}y - \frac{c}{b}z - \frac{d}{b} = y \quad (4.9)$$

$$\begin{bmatrix} x_0 & z_0 & 1 \\ \vdots & \vdots & \vdots \\ x_n & z_n & 1 \end{bmatrix} \begin{bmatrix} -a/b \\ -c/b \\ -d/b \end{bmatrix} = \begin{bmatrix} y_0 \\ \vdots \\ y_n \end{bmatrix}$$

$$-m_y = \frac{a}{b}$$

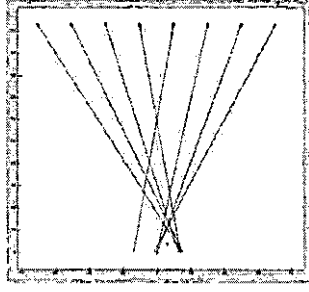
$$k_y = -\frac{c}{b}z_{iso} - \frac{d}{b}$$

$$y = -m_y x + k_y \quad (4.10)$$

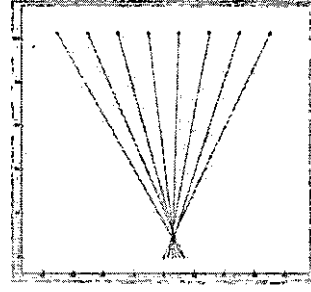
$$\begin{bmatrix} 1 & m_y \end{bmatrix} \begin{bmatrix} y \\ x \end{bmatrix} = k_y \quad (4.11)$$

As we can see from figure 4.4, by using equation 5.3 and equation 4.9 to estimate planes in figure 4.4(b) and 4.4(d) respectively we get and quite accurate x and y coordinate estimate. However, when you swap the choice of equations, even though they are mathematically identical, they make a huge numeric difference as shown in 4.4(a) and 4.4(b).

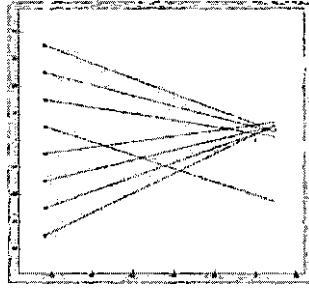
When estimating the x-y coordinate using least square we should keep in mind that least square assumes there is no observation error, it will only try to correct one side of the equation depending on how it is setup. With this in mind, we uses equation 4.8 for x coordinate estimation and 4.11 for y estimation. For the tubes on the diagonal planes, as we can see in fig4.5, they offers neither a good data for x nor y coordinate estimation as compared to fig 4.4 (b) and (d). So in order to utilize the diagonal tubes we have to rotate these tubes to either x or y plane, and get an estimation of a rotated x-y coordinate, then rotate the rotated x-y coordinate back



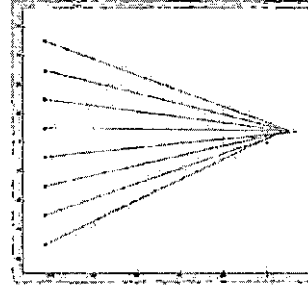
(a) *LS fit with y orientation.*



(b) *LS fit with x orientation.*



(c) *LS fit with x orientation.*



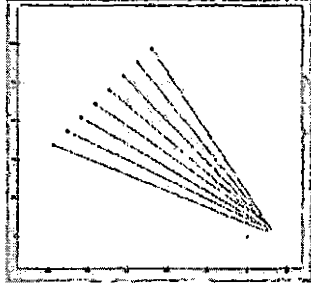
(d) *LS fit with y orientation.*

Fig. 4.4: Phantom modeling with distortion, showing differences in isocenter estimates due to how the LS equation is oriented.

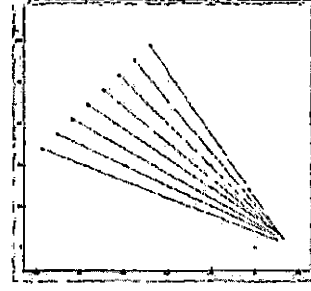
and average it with original x-y coordinate estimation.

In order to obtain a good estimate, we thus must separate the estimation of x and y, as well as rotate the diagonal oriented tube planes and then separate the estimation of x and y and rotate back. We refer to this algorithm as Rotated Separable Least Squares (RSLS). We now present the RSLS algorithm to estimate x-y coordinate of gradient isocenter as follows:

1. Use equation 5.3 to estimate tube planes for tubes at upper and lower surfaces.
2. Solve equation 4.8 for x and y, but only use x for x coordinate.
3. Use equation 4.9 to estimate tube planes for tubes at left and right surfaces.



(a) *LS using  $x$  orientation.*



(b) *LS using  $y$  orientation.*

Fig. 4.5: Phantom modeling with distortion, showing how diagonal tube planes without rotation do not improve the estimates produced.

4. Solve equation 4.11 for  $y$  and  $x$ , but only use  $y$  for  $y$  coordinate.
5. Rotate diagonal tubes  $\pi/4$ , and repeat steps 1-4.
6. Rotate  $x$ - $y$  coordinate obtained from previous step by  $-\pi/4$ .
7. Average the  $x$ - $y$  coordinate from previous step with  $x$ - $y$  coordinate calculated from step 2 and step 4 for final  $x$ - $y$  estimation.

Alternatively, after obtaining the plane equation parameters we can put everything into one matrix and do a one time estimation using either least square or total least square. In table 4.1, we can see the comparison of accuracy of estimating an isocenter at [4 4 3] using different methods. Least square tends to lean toward one coordinate more depends on setup, while total least square has an accurate and very balanced result due to the property that it will try to correct errors on both side of the equation. In the contrast, our method has best properties of both methods:

- It is accurate. For both  $x$  and  $y$  coordinate it does a better job than total least square, much better than least square's worst case and very close to least square's

	$\bar{x}$	$\sigma_x$	err	$\bar{y}$	$\sigma_y$	err
RSLS	3.9709	0.1068	0.0291	3.9677	0.1008	0.0323
LS	3.9950	0.1118	0.0050	3.9414	0.1011	0.0586
TLS	4.0800	0.1035	0.0800	4.0800	0.0964	0.0800

Tab. 4.1: Average of 200 runs using different methods for estimating the isocenter at [4 4 3] in the presence of symmetrical distortion

best case.

- It has very balanced result. Both x and y coordinates are very close the correct result equally just like total least square.
- It has very tight error boundaries. After 200 runs, it's error is tighter than standard least square.

Therefore, our estimation method is a good alternative to traditional least square or total least square methods. Although it might require more computation, it could be easily dealt by modern GPU computing. And due to the fact that each least square estimation has relative small matrix, and each estimation is independent of each other, it is very close to “embarrassingly parallel” type of problems and makes it easy to solve.

In table 4.1, the test is run using a symmetric x-y axis distortion. We can see that all three methods performed very well. RSLS method's result is slightly better than Total Least Squares (TLS), and one on y axis it is better than standard Least Squares method.

When the distortion is not symmetrical the issue of proper estimation becomes

	$\bar{x}$	$\sigma_x$	err	$\bar{y}$	$\sigma_y$	err
RSLs	3.8073	0.1117	0.1927	3.9838	0.1059	0.0162
LS	4.2191	0.1117	0.2191	3.8765	0.1003	0.1235
TLS	9.5744	0.2616	5.5744	8.6905	0.2393	4.6905

Tab. 4.2: Average of 200 runs using different methods for estimating the isocenter at [4 4 3] in the presence of non-symmetrical distortion

crucial. In table 4.2, we show the result of using non-symmetrical distortion in which the y direction was set to be twice the distortion in the x. In this test, TLS method's result is the worst, off by a few millimeters. Both LS and RSLs show comparable degradation of performance in x. LS shows degradation in the estimation of y as well, but RSLs, since it is separable, does not experience any degradation of it. Only the RSLs's result remains quite accurate. This shows the advantage of RSLs over the other two traditional methods.

#### 4.6 Conclusion

In this work, we developed a new numerical algorithm to accurately determine the gradient isocenter of MRI scanners based on a new distortion correction phantom. Knowledge of the gradient isocenter is an essential part of gradient-nonlinearity correction methods. We have shown that the method used in this work to estimate the gradient isocenter is a good alternative to more traditional estimation methods such as least squares and total least squares. The new algorithm is particularly suited when the image data are extremely sensitive to the presence of noise and asymmetric distortion. Using simulated (but realistic) distortion data, it was shown, that

the resulting estimated isocenter was within 0.2 mm of the actual gradient isocenter, leading to a better estimate than the currently used DICOM coordinate center.

## 5. DATA EXTRACTION

### *5.1 Introduction*

In order for our estimation to work we need to collect two different types of data for our calculations. One is the true geometric dimension of our phantom, the other is the corresponding distorted signal that represent those known geometric locations inside MR images. Some of these data can be relied on manufacture's measurement, while others would require us to extract information from various types of images to estimate the measurements. In this chapter we will discuss how we obtain each measurements and algorithm involved in those processes.

### *5.2 Measuring Water Tanks Distances Using CT Images*

#### *5.2.1 Introduction*

Due to the limitation of manufacture's equipments, water tank at each end can only be guaranteed that their surfaces are parallel to each other, their accurate distances between each other are unknown. We decided to perform a CT scan on the phantom, then collect each surfaces' data points through coronal view CT images. With enough data points on each surface, we should be able to have a good estimation of the distances with between each pair of surfaces.

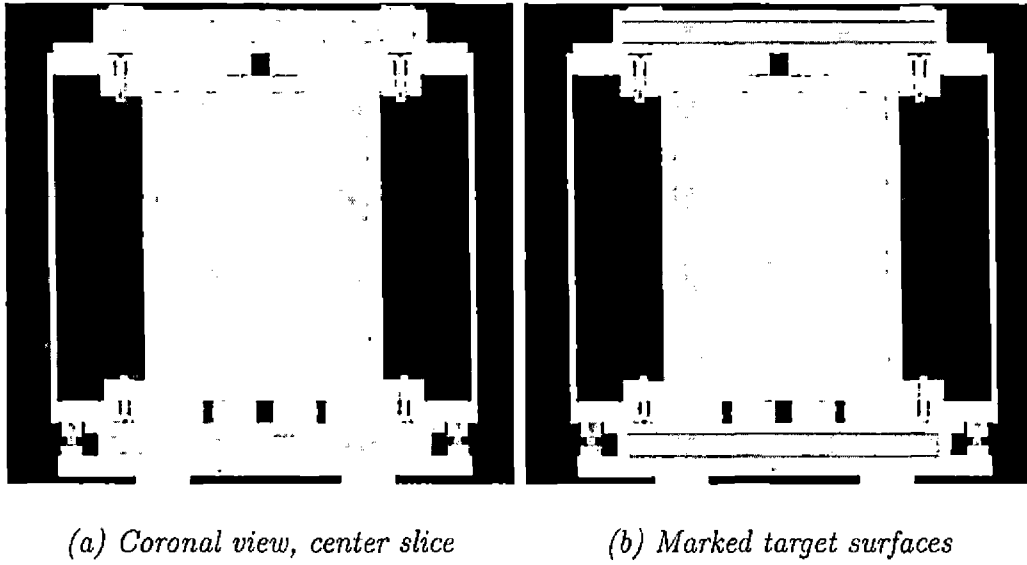


Fig. 5.1: Sample CT image in coronal view.

Figure 5.1 (b) indicates the target feature we are looking for inside a typical coronal view of CT image.

### 5.2.2 Canny Edges

The obvious method is to extract the data points is to apply an edge detection algorithm on the image, then iterate through the resulting edge image to collection the desired lines. However, the resulting edge image from this approach often contain fair amount of noise edges some of which overlap with the desired edges we are looking for. This problem is illustrated in figure 5.2, 5.3 and 5.4.

In figure 5.2(a), we can see that Matlab's canny algorithm with default parameter gives descent edges when applied to image #141. However, the same parameters will create many noisy edges in some other images, e.g. #270 in the same series in figure

5.3(c). Setting higher threshold is able to reduce those noisy edges as we can see in figure 5.3(c), but that threshold will eliminate some edges we are looking for as shown in 5.2(c).

To get rid of this noisy edges, different types algorithms might be involved, probably including validating all the edges in an image, which might involve multiple pass to the whole image, and in which case the process could be slowed down by factor of several times. So if there is a simpler and faster way, it would be preferred choice.

### 5.2.3 *Surface Location*

Since all objects we are looking for has a very uniform and distinct shape, we could start with finding a small regions each contains one object. In our case, the choice is very obvious. The objects we are looking for are four straight lines at fixed location and parallel to each other. For images that contain those objects, they should have them at almost exactly the same location with possibility of a few pixels offset due to potential tilt of the phantom during scan. If we choose a slice in the middle of the series, that should give us a relatively smaller overall error margin both above and below the surface location on that particular slice comparing to picking a slice at the beginning or at the end of the series which would give a relatively larger error on either above or below the surface location. Also the slice in the middle of series tends to have better quality. We would call this middle slice as surface location sample.

In the surface location sample, we would plot a histogram of gradient of the sum of middle 7 columns as shown in figure 5.5(a) and a histogram of intensity distribution as shown in figure 5.5(b). From figure 5.5(b), we can see that there are three very obvious

normal distribution in the graph. From left to right, they represent background noise signal, water signal and phantom tank signals respectively. In figure 5.5(c), a zoomed in picture of the region between water signal distribution and phantom tank distribution, we can see that two distributions' tails overlaps with each other. From the fact that the number of pixels in this overlap region is quite small and that this region is between two distributions, we can determine that most of them should be the pixels on the boundary between water and tank. So, according to ranges of two distributions as we can observe from the diagram, the range of difference between tank signal and water signal should be somewhere between 40 to 300. However, since the difference we are looking for is on the boundary of water and phantom tank, signals in those regions should tend to be close to each other. Therefore we should expect the to see spikes in gradient to be around  $\pm 40$ . In figure 5.5(a), we can clearly see six spikes that can be uniquely identified. Their values are -41.8404, 44.2372, -36.2271, 50.4055, -40.9654 and 29.8124, and they are right around the predicted range. Thus, we can identify them with high confidence that they are on each of the boundary between water and phantom tank.

With one pixel on each locations of the water and phantom tank boundaries are identified, we can also narrow down the location of each surface by specifying the surfaces are within the  $\pm 5$  rows of the row coordinate of each identified pixels. The  $\pm 5$  rows should give enough room for any horizontal or vertical tilts.

### 5.2.4 *Edge Detection On Local Surface Region*

After the regions of boundaries of water and phantom tank are extract we can proceed to extract the surface edge from these regions. The following issues are need to be resolved:

1. Identify the left and right boundaries of the edges.
2. Remove the noisy edges, and there are two types noisy edges:
  - (a) Noisy edges that are not in contact with the target edge.
  - (b) Noisy edges that are in contact with the target edge.

#### *Boundary Finding*

To detect the left and right boundary we plot the histogram of sum of intensities of each column across the region as well as the gradient for the intensity graph as shown in figure 5.6.

Upper pair of arrows in figure 5.6(a) indicates where the inside edges of the phantom tanks are, and the lower pair of arrows indicates how do those edges shows up in its gradient graph. The two small edges are identifiable with properties of value between 200 and 1000. We can identify them with this property for most of the slices. The transition from phantom tank to water become smoother on the slices more toward anterior or posterior in coronal view.

There are couple of issues with this approach.

- For images close to either edges of the two tanks, contrast ratio between water and tank material become very weak. As shown in figure 5.9, the transition from

tank to water become very smooth, and their gradient, therefore, become very small, and fallen out the filter range we specified. If we lower the range of the filter, it will pick up too many noise.

- For superior tank's outside surface, its regions also include the end part of tubes. Structure on those regions of tubes are fairly complex, which will result in frequent change of each column's total intensities in regions that have tubes.

However, with the slices that able to identify the edges, we can reconstruct majority of each water tank surface and they are more than enough for us to estimate the distances between each surfaces, especially with the assumption that they are all flat and parallel to each other.

### *Removing Noise*

We are going to remove the noise of the each edge in two steps.

1. Remove noisy edges that are unattached to target edges.
2. Filter out small edges sticking out of target edges.

Noisy edges unattached to target edges has one characteristic which is short. Since these edges are generated by noises, all observations has shown that they all tend to be very short in length due to lack of consistent pattern. To remove the noisy edges that are unattached to the target edges, we do the following steps:

1. Create an empty image that has the same size of the input image.
2. Iterate every pixel of input image

- (a) if current pixel in input image is not zero:
  - i. We recursively collect all the nonzero pixels from the input image and set those pixel values on the input image to 0.
- (b) If there has been an edge collected, we check the length of this group of pixels
  - i. If the length is less than a threshold, say, 15, we assume they are a noisy edge and complete ignore this group of pixels
  - ii. Otherwise, we will write these pixels' values to the image we initially created.

After following above steps, the resulting image will look like something like figure 5.8 (c).

At this stage, we will apply the boundary limit to this newly filtered edge, removing all the pixels beyond either left or right boundary. And this will left us with target edges with some small noisy edges sticking out as shown in figure 5.8 (d).

To filter these sticking edges out, we do the following steps:

1. Extract 2d coordinate information of every edge pixels, and fit them to a straight line, since we know our target edge is a straight line. We can setup the equation as:

$$\begin{bmatrix} columns & 1 \end{bmatrix} \begin{bmatrix} m \\ k \end{bmatrix} = \begin{bmatrix} rows \end{bmatrix} \quad (5.1)$$

where *columns* is column values of all edge pixels and *rows* is row values of all edge pixels. *m* and *k* will the line parameter of the straight line we are trying to fit into.

2. Group all edge pixels by their column value.
3. Iterate all column groups. We pick a pixel from each group having the minimum value of  $|Pixel_{row} - (m * Pixel_{column} + k)|$  and ignore the rest.
4. At the end we should have one pixel per column group left, they will be our final edge.

For testing we write out these filtered edges to original input image. We can see the result in figure 5.9 (a). For some edges, in some image we are unable to determine the left and right boundary. We will skip them as we have more than enough data with images that can gives us good edges. Figure Figure 5.9 (b) is an example where some edges are identifiable while others not.

### *Improvement*

#### 5.2.5 *Creating Surfaces*

Surface in 3D space can be represented by equation:

$$ax + by + cz + d = 0 \quad (5.2)$$

With somewhere between 50,000 70,000 data points for each surfaces, it's the best to use least square ( $Ax = b$ ) to estimate each surfaces' equation parameters. Considering the following fact:

1. Least square assumes that there is error in measurement but not observation, so it will only try to minimize error in A not b.
2. For every data point we only have measurement error in two axis, the third one is taking for granted from DICOM info. Though there should be some very

small error during CT image reconstruction as well, but that's not necessary to be consider here.

Since the image set we are dealing with is coronal view, which means it's the y-axis we are taking for granted, we are setting up our least square as follows:

$$\frac{a}{b}x + \frac{c}{b}z + \frac{d}{b} = -y \quad (5.3)$$

$$\begin{bmatrix} x_0 & z_0 & 1 \\ \vdots & \vdots & \vdots \\ x_n & z_n & 1 \end{bmatrix} \begin{bmatrix} a/b \\ c/b \\ d/b \end{bmatrix} = \begin{bmatrix} -y_0 \\ \vdots \\ -y_n \end{bmatrix} \quad (5.4)$$

With this setup, our estimated parameters for each planes are:

	$a$	$b$	$c$	$d$
surface 1	$-1.0617 \times 10^{-06}$	1	$-6.9880 \times 10^{-10}$	-2.0644
surface 2	$-3.8209 \times 10^{-06}$	1	$-2.3851 \times 10^{-9}$	-6.7681
surface 3	$3.2496 \times 10^{-06}$	1	$4.3242 \times 10^{-10}$	-4.8297
surface 4	$3.3399 \times 10^{-06}$	1	$1.2575 \times 10^{-10}$	-2.0644

Reconstructed surfaces can be see below:

Notice that in the YZ view in figure 5.10(a) (b) (c), all four surfaces are tilted. This is consistent with what we observed on sagittal reconstruction of this image set.

### 5.3 Extracting MR Tubes Centers from MR Images

#### 5.3.1 Introduction

There are total 64 MR tubes filed Copper Sulfate ( $CuSO_4$ ) places on the outer region of the phantom. We filled them with  $CuSO_4$  due to this solution has very good

magnetic susceptibility inside MRI scanner. They produce very strong signals in MR images which make them much easier to extract. Tubes can be purchased separately, and easy to replace if necessary. Tubes are sealed with silicon to prevent leaking and could stored vertically for a long period of time.

These tubes are used to estimate MRI scanner's gradient isocenter as well as calculate the x and y axis' correction parameters. To calculation correction parameter, we need both original accurate 3D locations and distorted 3D locations of each tubes. We can use tube holders' spacing specified in phantom's specification to determine their corrected locations since these holders are precision made. So the missing information are distorted tubes locations. MRI's distortion is nonlinear, which means the 3D shifts at different locations are different. The way we extract tubes' distortion is by analyzing the axial scan/reconstruction of the phantom to determine a starting and ending slice of those tubes, and for every slices in between them, we find the center of the each tube. Each bent tube in MR images can be viewed as series. We will use these centers in later calculation of correction parameters.

### 5.3.2 *Range*

This section describes how to determine the first and the last axial slices that are used to extract tube centers.

Tube holders at both end of the MR tubes will cause the regions of the tubes inside the tube holder to shift. Depending on how the original scan is performed, the shifts' direction may vary. If the original scan is done in axial direction, the the shift will occur inside xy plane; if the original scan is performed in sagittal direction the shift

will occur on z-axis. So this means that we cannot use the signal from the regions where tube holders are at.

One way to determine where the tube holders' z-axis location is to find the middle water tank boundaries. Tube holder is usually at least 5mm away from each tank surfaces in MR images. So after finding the location of two water tank surfaces we can add or subtract 4mm as two boundaries. For every axial slices, we will check it's z-axis location to see if that slice is between the boundary, if it is, we will continue to process the slice, otherwise we will ignore it.

To find a accurate middle tank surfaces, we can work on either coronal or sagittal series, and use the following steps:

1. Average the middle slice of the series with its two adjacent slices to produce a sample slice. This way we can get rid of some noise and would give a more reliable result.
2. In the sample slice, we average middle 3 columns of pixels to produce a sample column.
3. Produce a gradient for the sample column.
4. The top surface of the middle water tank could be set to be the first peak in second half of the data that is greater than 150; and the bottom surface of the water tank could be set to the last peak in the first half that's lower than -150.
5. Two pixels will be used for calculating the z-axis location of the two tank surfaces. Their row values are the two values we calculated from previous step respectively, and their column values are both middle column of the middle slice of this series.

6. Two pixels will be converted into 3D DICOM coordinate using DICOM affine formula. The one with positive z coordinate will be added 4mm and the one with negative z coordinate will be subtract 4mm. These two z coordinates defines a range which axial slices used to extract MR tubes centers should be in.
7. To validate a axial slice, we use the ImagePatientPosition parameter to see if the slice is in the range.

### 5.3.3 Tube Centers Extraction

This section describes the method used in tube center extraction.

A typical axial view of phantom in MR images looks like this:

The strategy to extract tube centers is to use one slice to produce a series of masks which specified the tube locations. For reset of the slices, we use the masks to extract regions where tubes are at and process each region separately. There are several advantage of doing this:

- This method will make the whole process runs a lot faster due to significant less amount of pixels needed to process.
- It also has a lot potential to run much more faster. Once a set of masks is produced from a image, not only a number of images following that slice could be processed simultaneously, 64 regions in each images could also be processed at the same time after they are extracted.
- It will be less error prone as well, due to masks narrows down the problem regions.

### *Mask Extraction*

This section describes how the masks are produced.

The following steps are used to extract a set of tube mask from an axial MR images within the range we have calculated previously.

1. Use a threshold to produce a binary image that only contains tube signals. Due to the good susceptibility of  $CuSO_4$  solutions, signals from solutions inside MR tubes are much higher than other regions of in the same image.
2. Apply canny edge detection on the binary image produced from previous step.  
Note: Applying canny directly on original image with high threshold will also yield a good quality edge images with much smaller circles.
3. Masks of tubes at top row, bottom row, left column and right column are generated first. for top row:
  - (a) Iterate the the top left region of the image, sweeping row wise from left to right to search for a pixel that belongs to left most tube on top row.
  - (b) Once an edge pixel is found, all the edge pixels of the this tube will be collected, i.e. record and remove from the image. And a center of the tube is computed using steepest descent method.
  - (c) Use the center calculated from previous method as a starting point and walk the pixels on the same row to the right to obtain 7 other tube centers of top row by repeating previous steps.
4. Use similar method that obtained centers of top row to obtain bottom row, left column and right column. For bottom row, lower right region of the image are

searched initially, sweeping from right to left, once the first tube center is found, algorithm traverse to left to collect the rest tube; for left column, top left region is swept column wise from up to down, after finding the first center, algorithm traverse down ward on the same column to search for other tubes. for right column, bottom right region is swept column wise from bottom to top, after finding the first center, algorithm traverse upward to search for other tubes.

5. For diagonal tubes, similar initial search is used to look for the first pixel of the first tube. When looking remaining tubes, row wised sweeping is motion is used.
6. After a center is found, a square region is allocated for a mask for that tube. In total, there are 64 masks extracted from on image. Each region will have it's top left coordinate on the image as well as width and height.

Center calculation is using steepest descent. Several other algorithms are tested, such as, weighted average, least square, but steepest descent has the best result among the three.

### *Center Extraction Using Masks*

With a set of mask is extracted, it would much easier to extract centers on other images with the masks:

1. Using each region's top left corner coordinate and it's width and height, 64 much smaller regions only containing tubes can be extracted.
2. Each region can use the same edge algorithm used earlier step, then extract pixels and calculate the centers. Center coordinate in the region will add to the

top left corner coordinate to become a coordinate in original image.

## *5.4 Extracting Water Tank Edges From MR Images*

### *5.4.1 Introduction*

Water tank edges in MR images contains the z-axis distortion information. Combining with water tank edges in CT images, z-axis correction parameters could estimated using least square fitting method.

Due to the similarity in physical location of the interested data points, algorithm used in water tank edge extraction from CT images is a good candidate. However, there are some issue preventing that algorithm to be applied directly on water tank edge extraction from MR images.

1. There are much more considerable noises in MR images than in CT images. Due to the length of the phantom is slightly longer than the internal length of the headcoil, one water tank is slightly outside of the headcoil. This will results a much noise region on the water tank appear in lower region of MR images, as shown in figure 5.12.
2. Unlike CT images, the surfaces in MR images are curved. So we cannot use the same line fitting method we used in CT images water tank edges extraction.
3. Unlike CT images, we need as much data points as possible on each surface. Especially those ones on the edge.

#### 5.4.2 Algorithm

The algorithm used in water tank extraction in MR images is a modification of water tank extraction in CT images, it can be described as follows:

1. Find left and right boundaries. The algorithm of finding left and right boundary is the same as as water tank edges extraction in CT images, except we only need to find the boundaries for top tank's lower surface. This is because before final MRI scan, the phantom is already aligned, MR tubes should be quite parallel to the z-axis, and all four surfaces left and right boundary should be extremely close. In fact, top tank's lower surface's left and right boundary should be wider than other surfaces. This tight bound is sufficient for rest of the algorithm to work well.
2. For each surface, instead of using canny algorithm to find initial raw edge, algorithm will iterate from left boundary to right boundary to analyze the histogram of each column, and pick the maximum peaks with the highest value as a edge point. As shown in figure 5.13.
3. The resulting edge from previous step is very noisy. The following steps will be use to remove the noises.
  - (a) Remove disjointed short edges.
  - (b) By analyzing the gradient histogram, remove large disjointed edges.
  - (c) By analyzing the gradient histogram, remove short bumps in noisy edge.
  - (d) By analyzing the gradient histogram, remove all the sharp peaks.

The algorithm used to parse the gradient histogram is described in figure 5.14.

Edge result after each step are shown in figure 5.15.

Using this method, the final surface extracted from MR images for lower tank lower surface is shown in figure 5.16

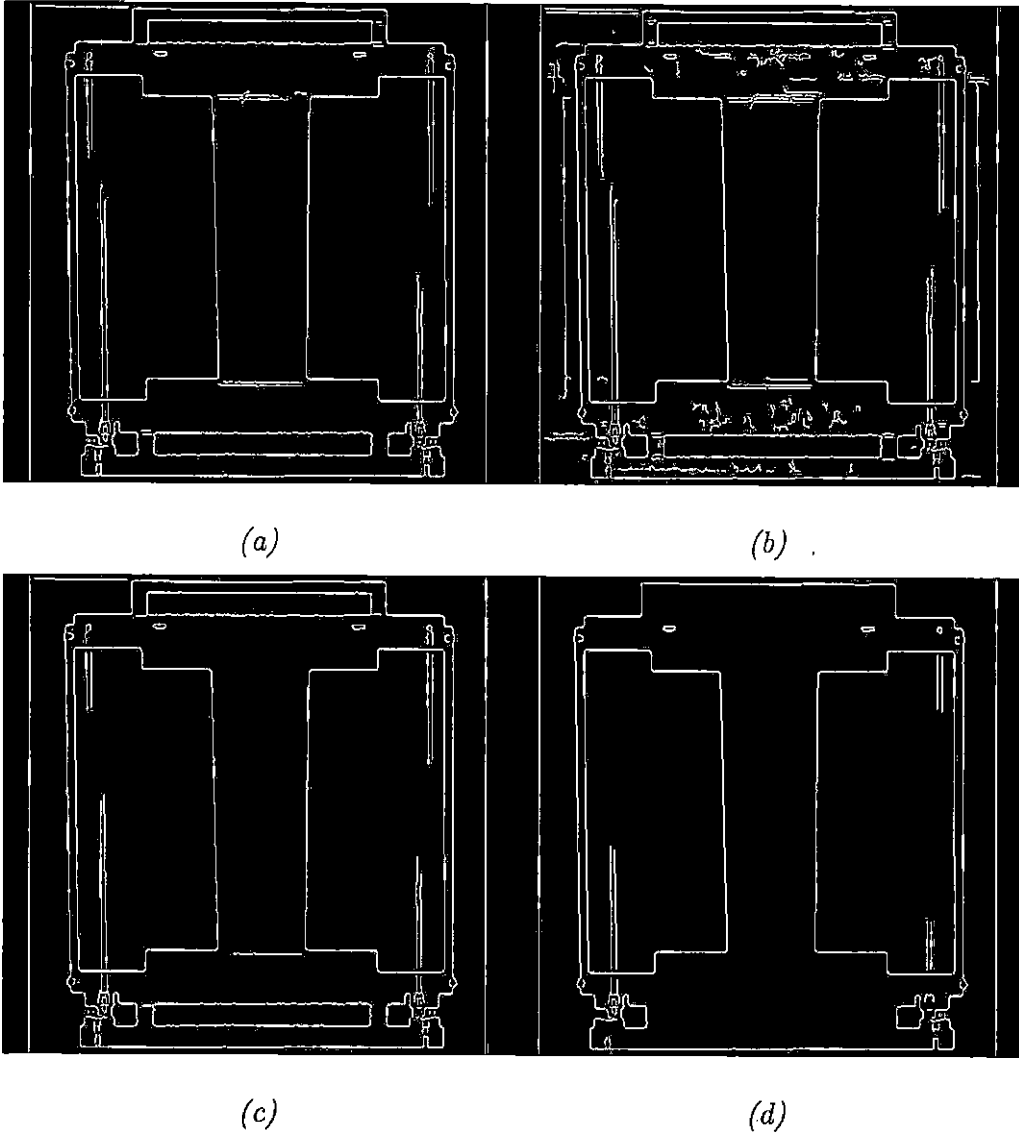


*Fig. 5.2:* Canny algorithm applied to coronal sequence 141 with different parameters: (a) Default parameters (b) Low threshold 0.01, high threshold 0.02 (c) Low threshold 0.02, high threshold 0.04 (d) Low threshold 0.05, high threshold 0.1

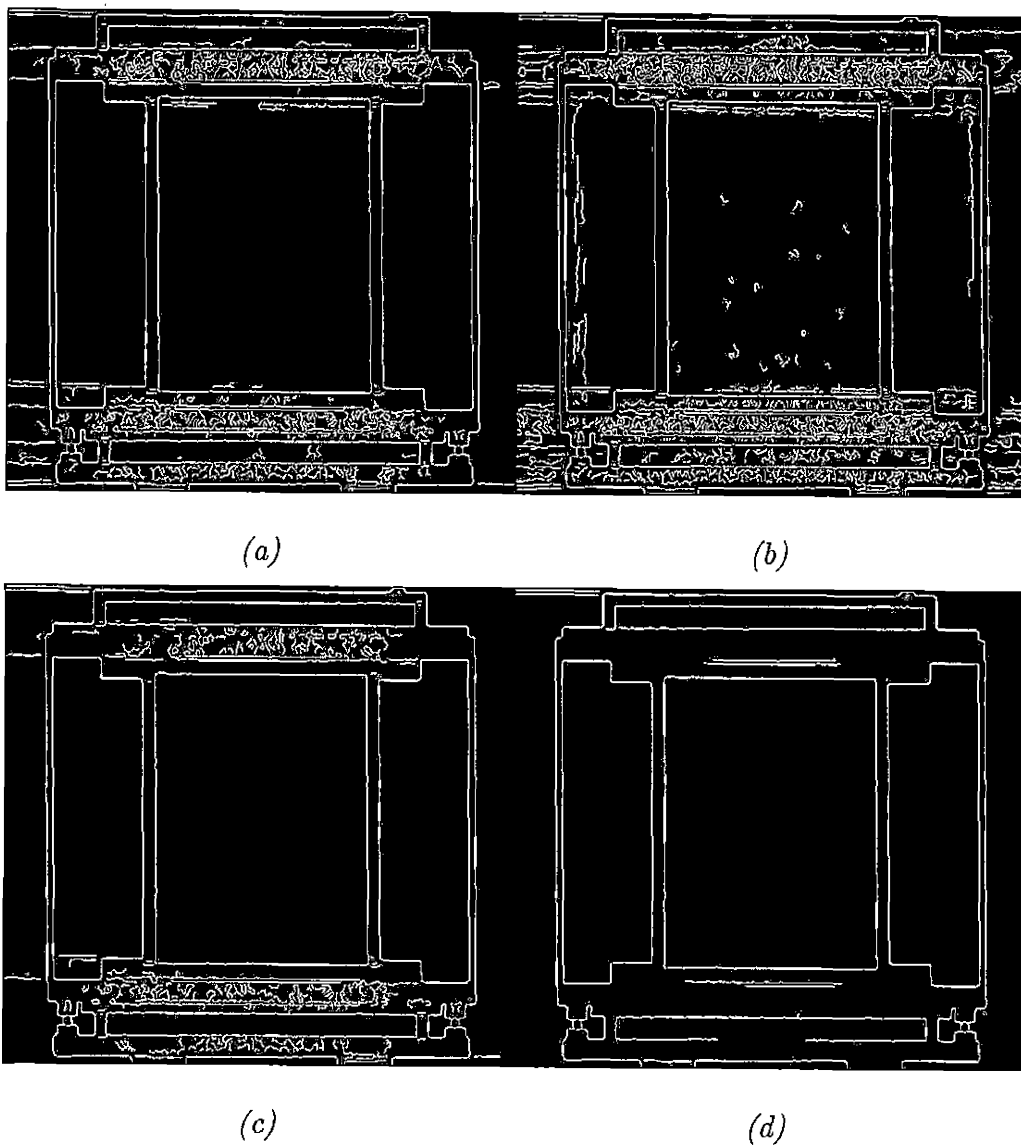


*Fig. 5.3:* Canny algorithm applied to coronal sequence 270 with different parameters: (a) Default parameter (b) Low threshold 0.01, high threshold 0.02 (c) Low threshold 0.02, high threshold 0.04 (d) Low threshold 0.05, high threshold 0.1

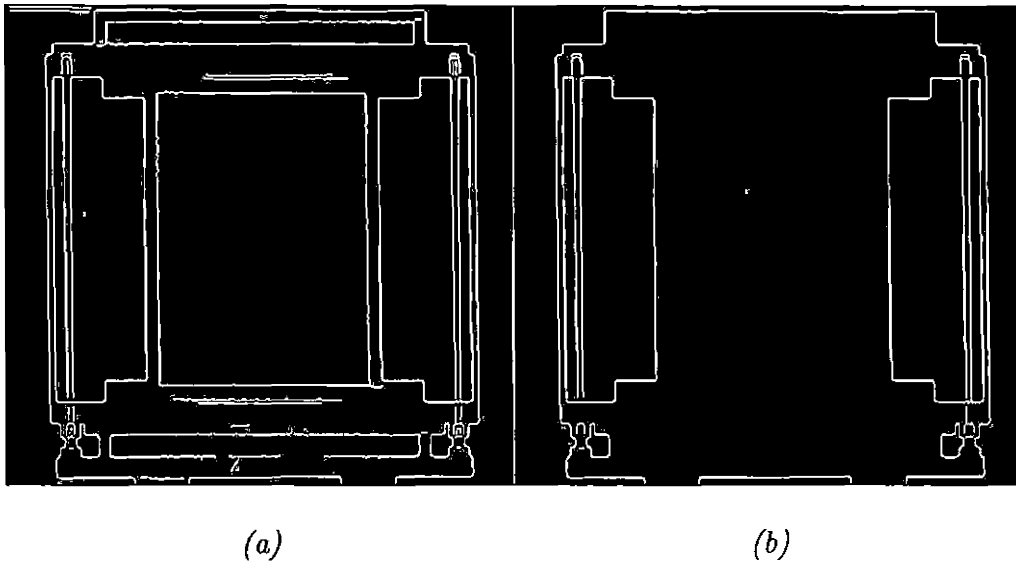


Fig. 5.4: Canny algorithm applied to coronal sequence 276 with different parameters: (a) Low threshold 0.02, high threshold 0.04 (b) Low threshold 0.05, high threshold 0.1

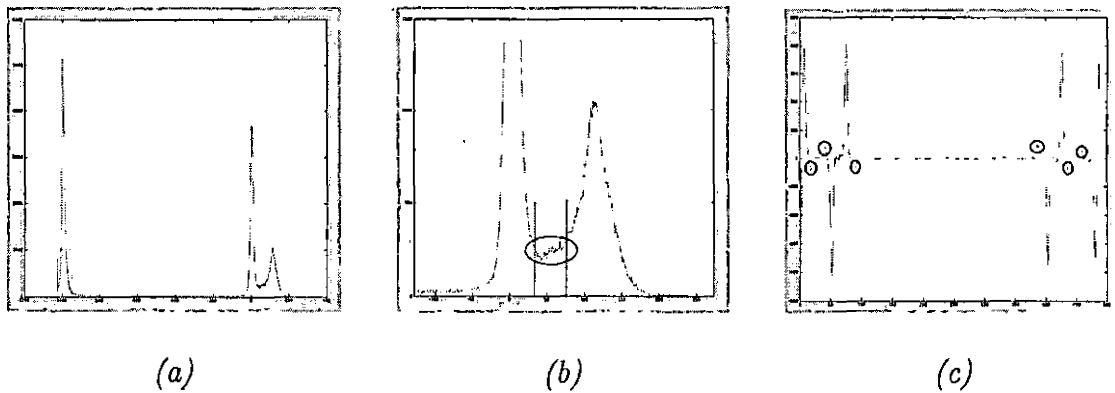


Fig. 5.5: Histograms of middle column of middle slice of a coronal series: (a) mid slice intensity histogram (b) Marked overlap region (c) mid slice surface locations

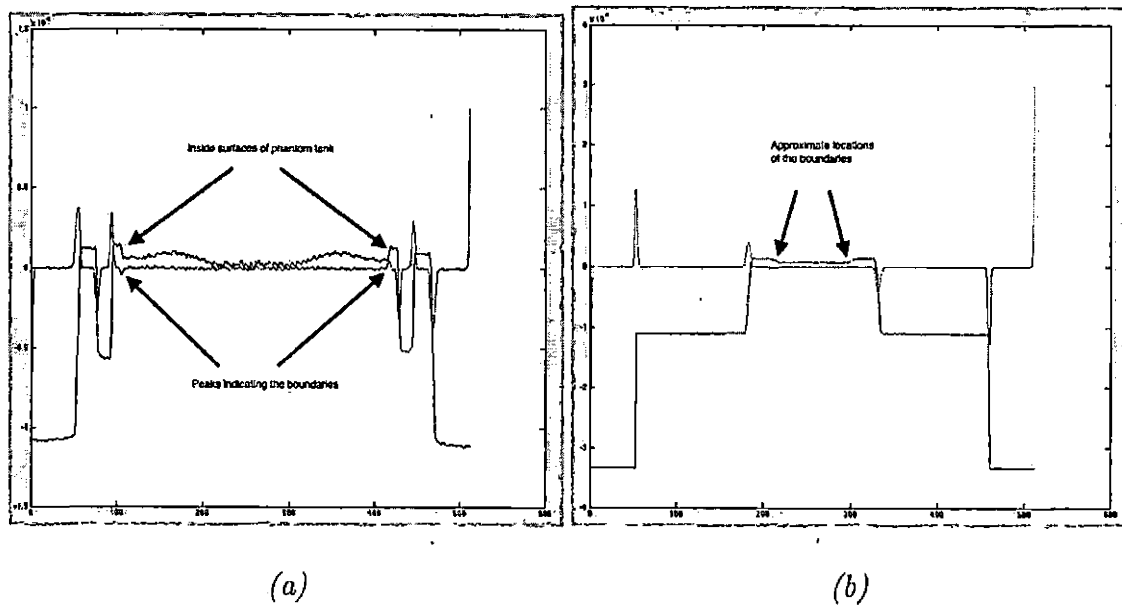


Fig. 5.6: Histogram for boundary detection: (a) inferior tank inside edge of #270 (b) superior tank outside edge of #100

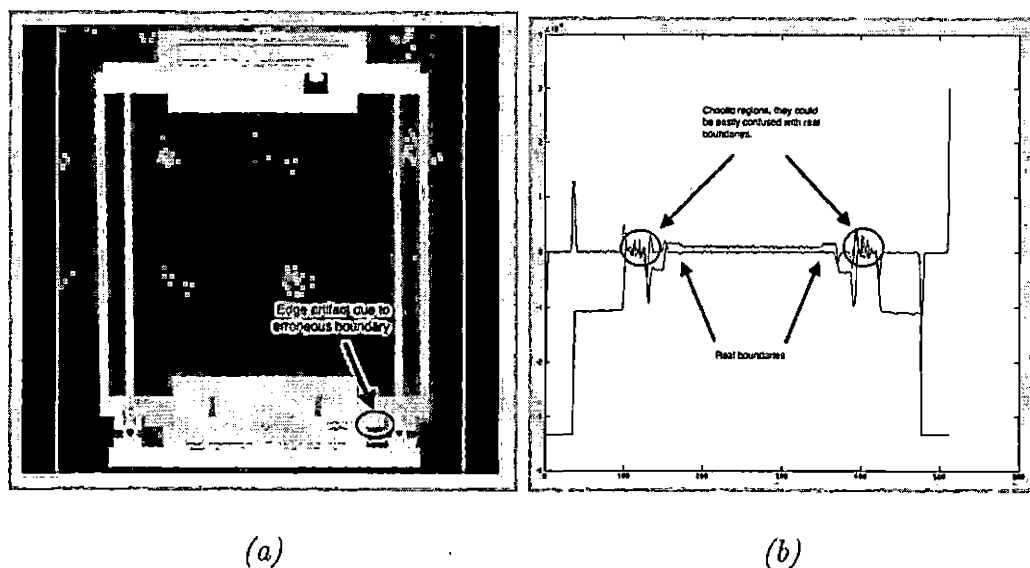


Fig. 5.7: Superior outside surface artifacts: (a) Extra edge caused by tube section (b) Histogram for superior outside surface of the same image

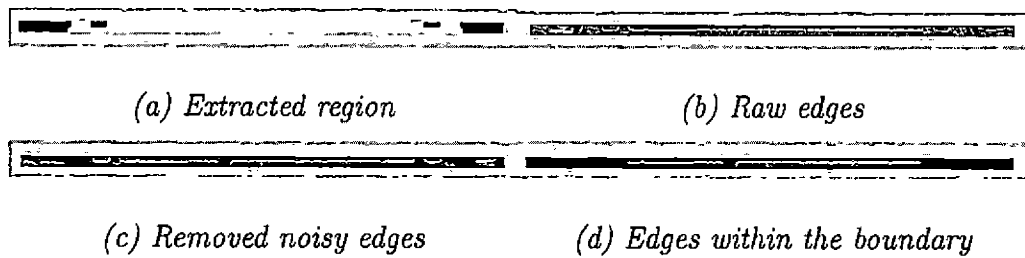


Fig. 5.8: Edge extraction intermediate results on image sequence #270's inferior tank inside edge

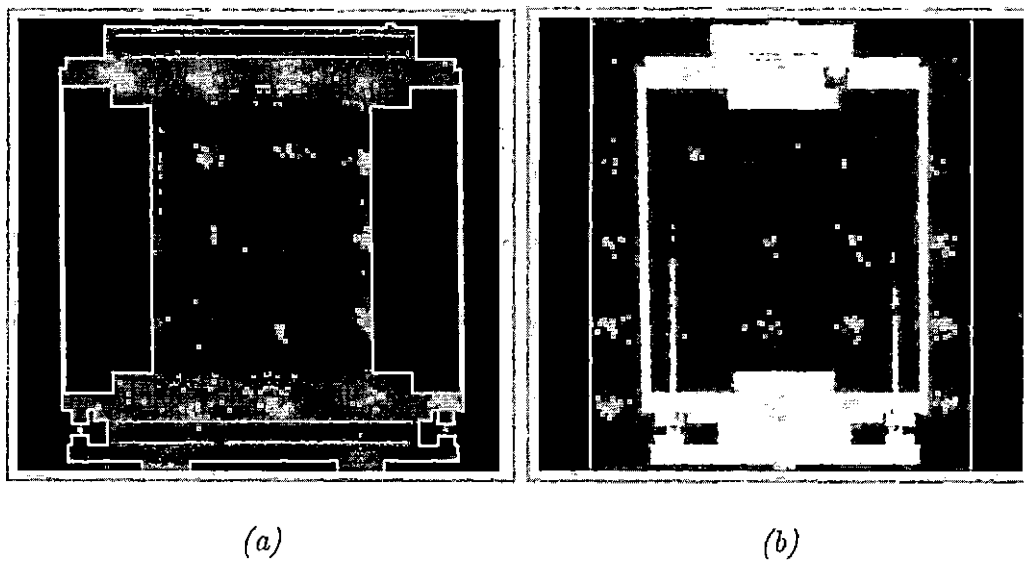
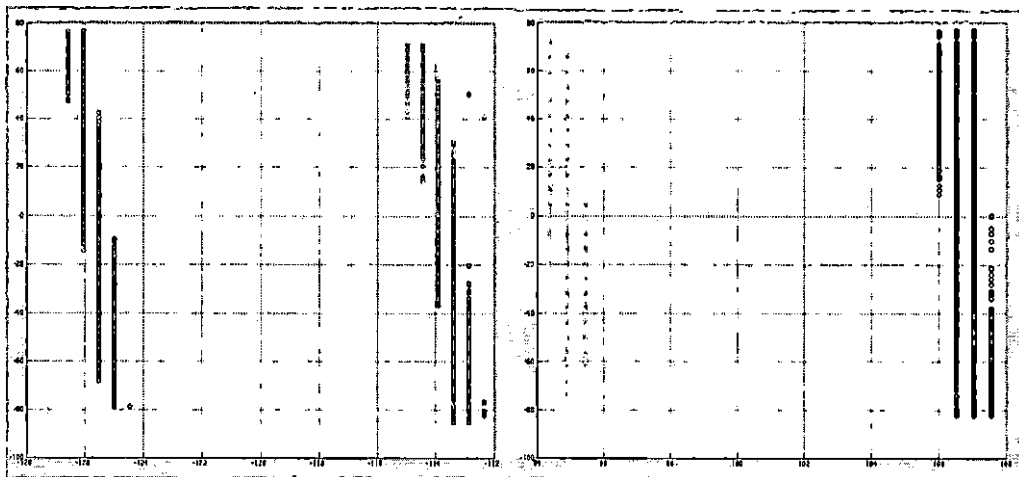
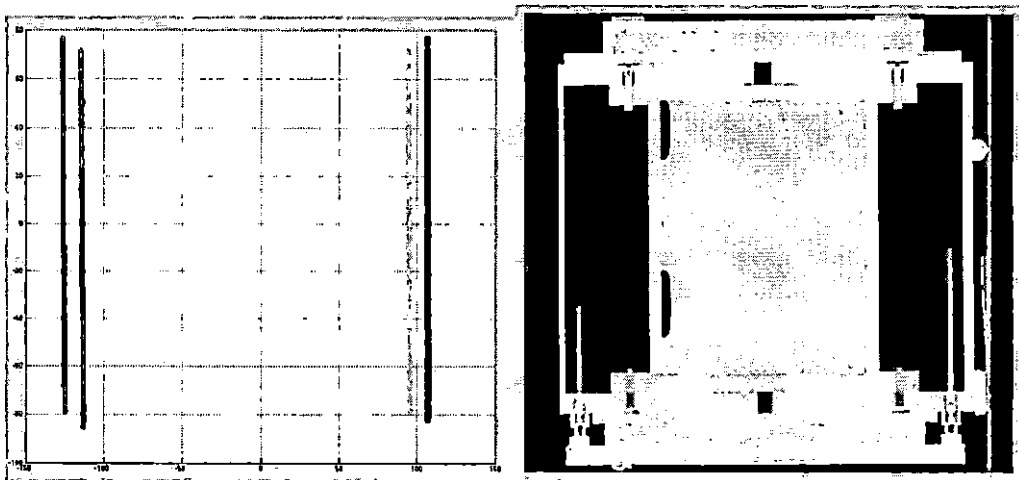


Fig. 5.9: Final edge results: (a) Edge result on image sequence #270 (b) Edge result on image sequence #100



(a)

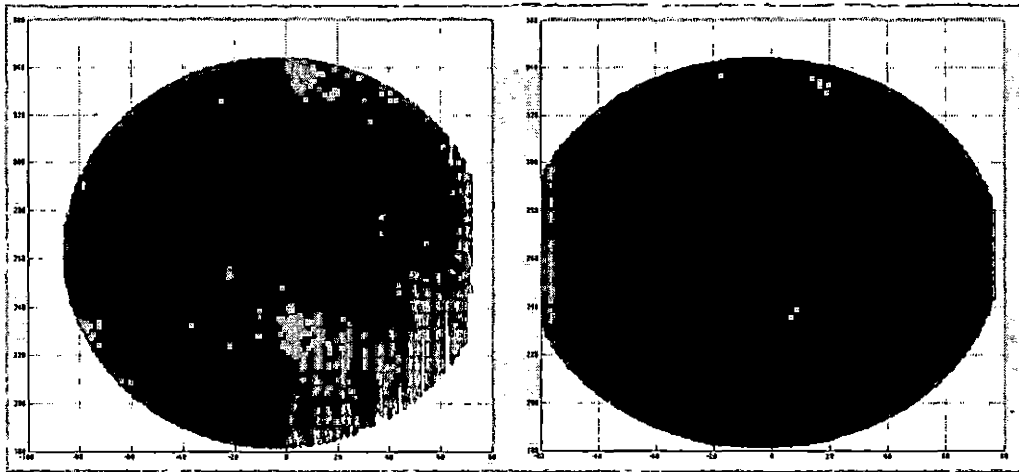
(b)



(c)

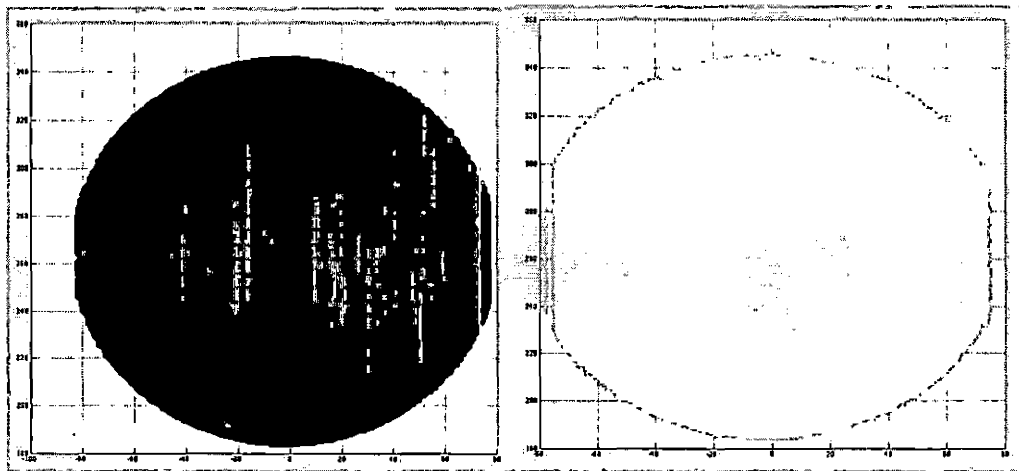
(d)

Fig. 5.10: Water tank surfaces reconstruction from CT scan, YZ view



(a)

(b)



(c)

(d)

Fig. 5.11: Water tank surfaces reconstruction from CT scan, XY view

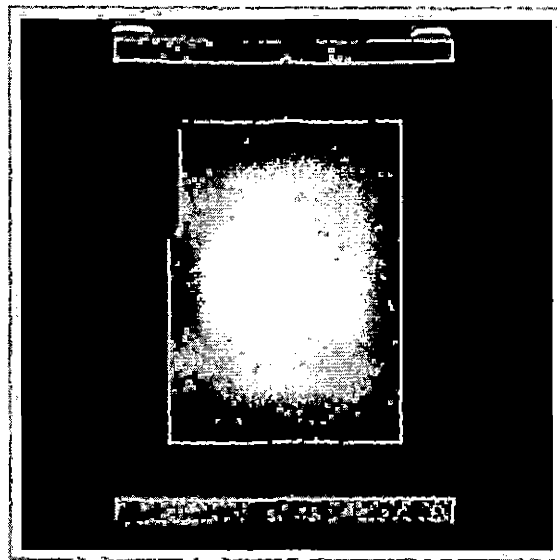


Fig. 5.12: Noisy MR images, especially the lower tank

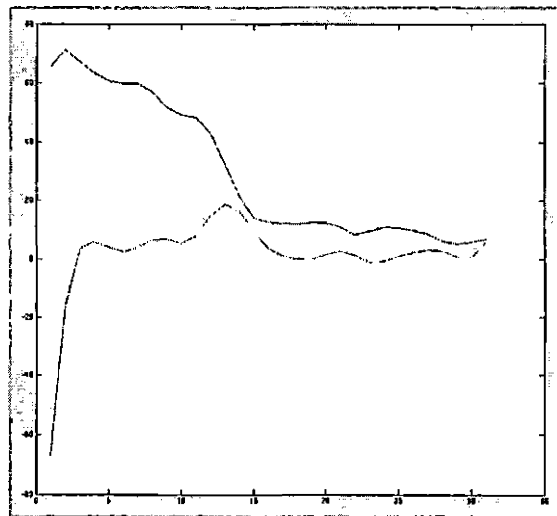


Fig. 5.13: Histogram for finding edge points

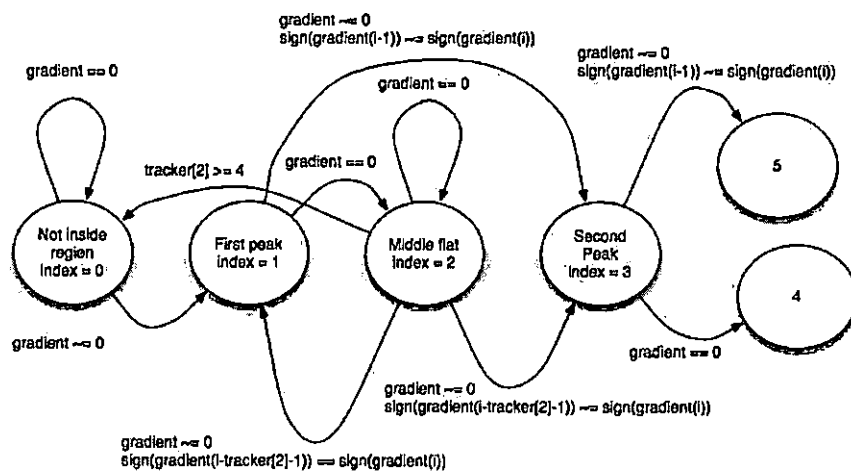


Fig. 5.14: gradient histogram state machine

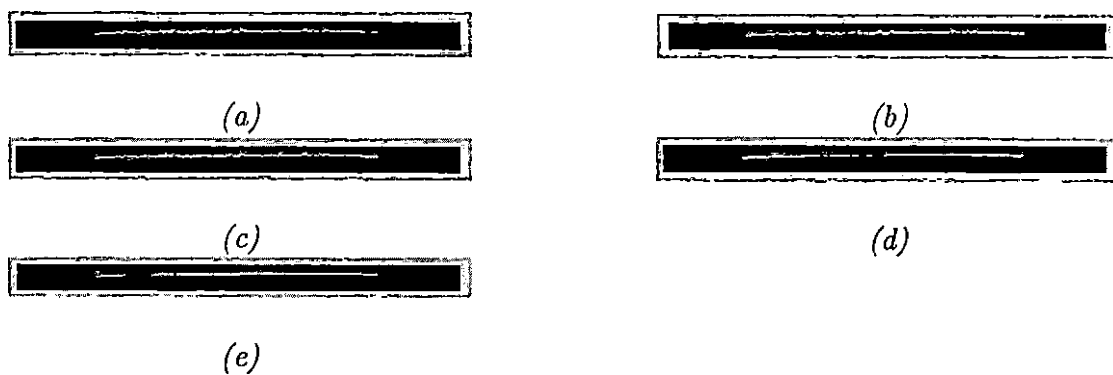


Fig. 5.15: MRI surface intermediate edge results: (a) Raw edge (b) after removing short edges (c) after removing large bumps (d) after removing peaks (e) final edge

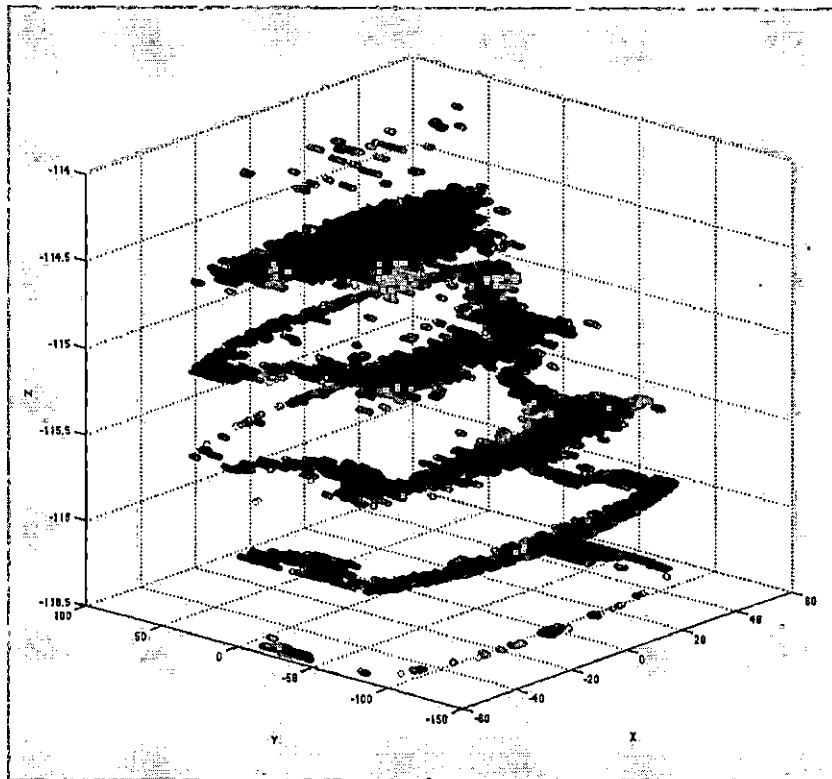


Fig. 5.16: Lower tank lower surface result.

## 6. DISTORTION CORRECTION PARAMETERS CALCULATION

### 6.1 Introduction

With both original measurements of the phantom and distorted data points, distortion or correction parameters can now be calculated

$$\bar{x}_i = x_i(1 + K_{x_0}(x_i^2 + y_i^2) + K_{x_1}z_i^2 + K_{x_2}z_i^2(x_i^2 + y_i^2) + K_{x_3}(x_i^2 + y_i^2)^2 + K_{x_4}z_i^4) \quad (6.1)$$

$$\bar{y}_i = y_i(1 + K_{y_0}(x_i^2 + y_i^2) + K_{y_1}z_i^2 + K_{y_2}z_i^2(x_i^2 + y_i^2) + K_{y_3}(x_i^2 + y_i^2)^2 + K_{y_4}z_i^4) \quad (6.2)$$

$$\bar{z}_i = z_i(1 + K_{z_0}(x_i^2 + y_i^2) + K_{z_1}z_i^2 + K_{z_2}z_i^2(x_i^2 + y_i^2) + K_{z_3}(x_i^2 + y_i^2)^2 + K_{z_4}z_i^4) \quad (6.3)$$

where  $(\bar{x}_i, \bar{y}_i, \bar{z}_i)$  and  $(x_i, y_i, z_i)$  represent distorted and corrected data sets. If  $(\bar{x}_i, \bar{y}_i, \bar{z}_i)$  is distorted data set,  $K_{x_i}, K_{y_i}, K_{z_i}$  would be distortion parameters, i.e. parameters used to distort original phantom data. If  $(\bar{x}_i, \bar{y}_i, \bar{z}_i)$  and  $(x_i, y_i, z_i)$  are swapped,  $K_{x_i}, K_{y_i}, K_{z_i}$  would work as correction parameters, i.e. parameters used to convert distorted data points into their original position. In this case, what need to be calculated is correction parameters which will be used to correct the distortions inside MR images.

Both  $(x_i, y_i, z_i)$  and  $(\bar{x}_i, \bar{y}_i, \bar{z}_i)$  have to be in DICOM coordinate, i.e. relative coordinate from gradient isocenter. The gradient isocenter computed in early chapters are using data points extracted from MR images, so it can be used to convert data

points from MR images into DICOM coordinate, but not the corrected data.

## 6.2 XY Axis Distortion Correction Parameters Calculation

This section describes how to setup and calculate the X and Y axis correction parameters.

Consider using two data points from two separate MR tubes in the same xy plane, two equations could be setup:

$$\bar{x}_0 = x_0(1 + K_{x_0}(x_0^2 + y_0^2) + K_{x_1}z_0^2 + K_{x_2}z_0^2(x_0^2 + y_0^2) + K_{x_3}(x_0^2 + y_0^2)^2 + K_{x_4}z_0^4) \quad (6.4)$$

$$\bar{x}_1 = x_1(1 + K_{x_1}(x_1^2 + y_1^2) + K_{x_1}z_1^2 + K_{x_2}z_1^2(x_1^2 + y_1^2) + K_{x_3}(x_1^2 + y_1^2)^2 + K_{x_4}z_1^4) \quad (6.5)$$

where  $(x_0, y_0, z_0)$  and  $(x_1, y_1, z_1)$  are DICOM coordinates of the two points from distorted space, which are known, and  $(\bar{x}_0, \bar{y}_0, \bar{z}_0)$ ,  $(\bar{x}_1, \bar{y}_1, \bar{z}_1)$  are DICOM coordinates of two points from corrected spaces which are unknown. However, the exact distance of tube spacings are known, as well as the distance between opposite side of tubes. So  $(\delta x_{0,1}, \delta y_{0,1}, \delta z_{0,1})$  can be calculated using

$$(\delta x_{i,j}, \delta y_{i,j}, \delta z_{i,j}) = (\bar{x}_i, \bar{y}_i, \bar{z}_i) - (\bar{x}_j, \bar{y}_j, \bar{z}_j) \quad (6.6)$$

where  $i, j$  should belong to the same row of tubes for calculating X-axis correction parameters or should belong to the same column of tubes for calculating Y-axis correction parameters. figure 6.1 shows how the pairing is done for x, and y axis.

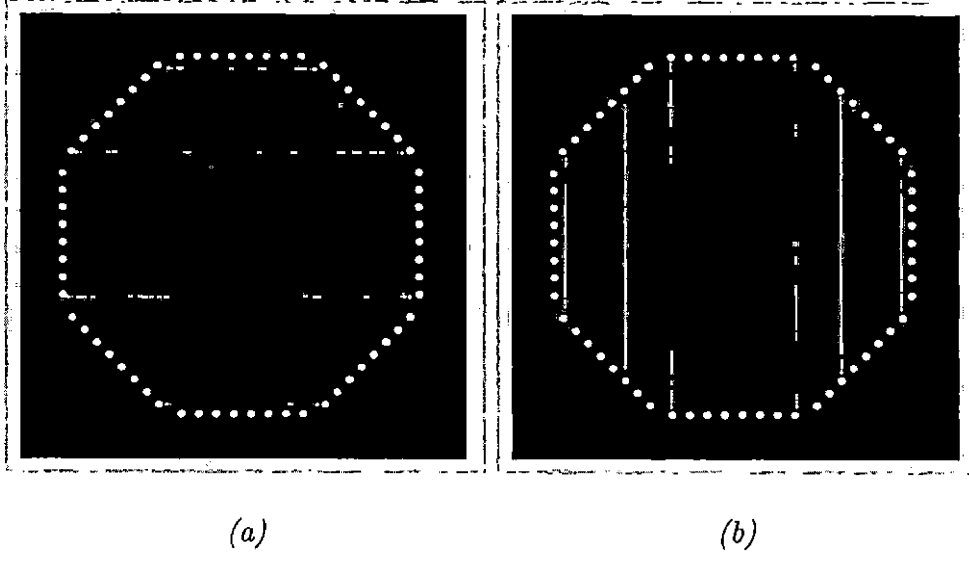


Fig. 6.1: Pairing of MR tubes. (a) Pairing for X-axis (b) Pairing for Y-axis

For each pairing, a new formula is produced.

$$\begin{aligned}
\delta \bar{x}_{ij} = & \delta x_{ij}(1 + K_{x_0}((x_i^2 + y_i^2) - (x_j^2 + y_j^2))) + \\
& K_{x_1}(z_i^2 - z_j^2) + \\
& K_{x_2}(z_i^2(x_i^2 + y_i^2) - z_j^2(x_j^2 + y_j^2)) + \\
& K_{x_3}((x_i^2 + y_i^2)^2 - (x_j^2 + y_j^2)^2) + \\
& K_{x_4}(z_0^4 - z_j^4))
\end{aligned} \tag{6.7}$$

$$\begin{aligned}
\delta \bar{y}_{ij} = & \delta y_{ij}(1 + K_{y_0}((x_i^2 + y_i^2) - (x_j^2 + y_j^2))) + \\
& K_{y_1}(z_i^2 - z_j^2) + \\
& K_{y_2}(z_i^2(x_i^2 + y_i^2) - z_j^2(x_j^2 + y_j^2)) + \\
& K_{y_3}((x_i^2 + y_i^2)^2 - (x_j^2 + y_j^2)^2) + \\
& K_{y_4}(z_0^4 - z_j^4))
\end{aligned} \tag{6.8}$$

### 6.3 Z Axis Distortion Correction Parameters Calculation

Similarly to xy correction, we pair up surfaces of water tanks. Figure 6.2, show the pairing.

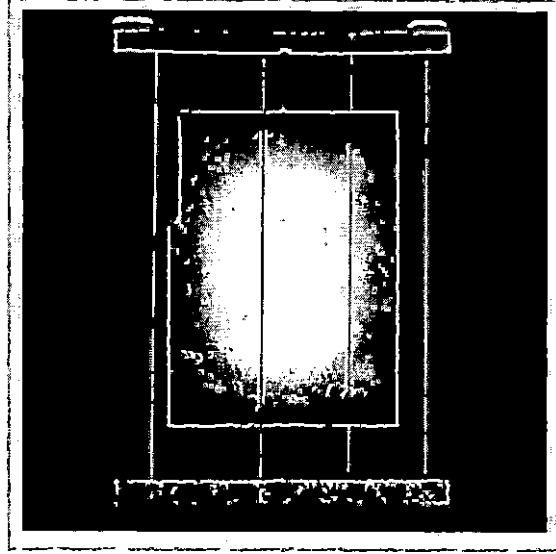


Fig. 6.2: Pairing of tank surfaces.

And the formula we used for z axis correction is:

$$\begin{aligned}\delta z_{ij} = & \delta z_{ij}(1 + K_{z0}((x_i^2 + y_i^2) - (x_j^2 + y_j^2)) + \\ & K_{z1}(z_i^2 - z_j^2) + \\ & K_{z2}(z_i^2(x_i^2 + y_i^2) - z_j^2(x_j^2 + y_j^2)) + \\ & K_{z3}((x_i^2 + y_i^2)^2 - (x_j^2 + y_j^2)^2) + \\ & K_{z4}(z_i^4 - z_j^4))\end{aligned}\tag{6.9}$$

## 7. SUMMARY AND CONCLUSION

In summary, all major goals of this thesis has been achieved:

1. A new phantom has been designed and manufactured which accurately captures the distortions inside MR images of a 3T MRI scanner
2. An algorithm was developed to calculate the gradient isocenter of the magnetic field of a 3T MRI scanner. Simulated results have shown that this algorithm worked quite accurately.
3. Several algorithms were also developed to extract required geometry information from CT and MR images for MRI distortion correction.
4. Finally, an algorithm was developed to calculate the distortion correction parameters using the phantom features extracted from the CT and MR images.

In the near future, further tests will be perform to explore the accuracy and limitations of this distortion correction algorithm developed in this thesis. There are other sources of geometric distortions in MRI images that need to be considered, including magnetic susceptibility distortion and chemical shift. Lastly, one should compare the performance of the correction algorithm developed in this thesis with that of intrinsic distortion correction algorithms that are included in the scanner software.

## REFERENCES

- [1] S.J. Doran, L. Charles-Edwards, S.A. Reinsberg, and M.O. Leach MO. A complete distortion correction for MR images: I. Gradient warp correction. *Phys. Med. Biol.*, 50:1343–1361, 2005.
- [2] D. Kondziolka. Functional radiosurgery. *Neurosurgery*, 44:12–20, 1999.
- [3] S. Langlois, M. Desvignes, J.M. Constans, and M. Revenu. MRI geometric distortion: a simple approach to correcting the effects of non-linear gradient fields. *J. Magn. Reson. Imaging*, 9:821–831, 1999.
- [4] T.S. Lee. Software-Based Gradient Nonlinearity Distortion Correction. Master’s thesis, California State University San Bernardino, December 2006.
- [5] T.S. Lee, K.E. Schubert, and R.W. Schulte. Gradient Non-Linearity Correction of MR Images for Functional Radiosurgery. In *ICIS-COMSAR ’06: Proceedings of the 5th IEEE/ACIS International Conference on Computer and Information Science and 1st IEEE/ACIS International Workshop on Component-Based Software Engineering, Software Architecture and Reuse*, pages 338 – 344, Honolulu, Hawaii, USA, July 10-12 2006. IEEE Computer Society.
- [6] T.S. Lee, K.E. Schubert, and R.W. Schulte. Software Development For Correction Of Gradient-Nonlinearity Distortions In MR Images. In P.P. Dey, M.N.

- Amin, and T.M. Gattton, editors, *Proceedings of the International Conference on Computer Science and its Applications*, pages 338 – 344, San Diego, 2006. US Education Service.
- [7] T.S. Lee, K.E. Schubert, and R.W. Schulte. Computational Algorithm for Modeling and Correction of Gradient Nonlinearity Distortions in Magnetic Resonance Imaging. In Sio-Long Ao, editor, *Proceeding of the World Conference of Engineering and Computer Science*, pages 210 – 215, San Francisco, 2008. Harvard School of Engineering and Applied Sciences, Harvard University, USA.
  - [8] T.S. Lee, K.E. Schubert, and R.W. Schulte. Software-Based Algorithm for Modeling and Correction of Gradient Nonlinearity Distortions in Magnetic Resonance Imaging. In Sio-Long Ao, editor, *IAENG Transactions on Electrical and Electronics Engineering*, pages 210 – 215, San Francisco, 2008. Harvard School of Engineering and Applied Sciences, Harvard University, USA.
  - [9] J. F. Schenck. The Role of Magnetic Susceptibility In Magnetic Resonance Imaging: MRI Magnetic Compatibility of the First And Second Kind. *Medical Physics*, 23(6):815–850, 1996.
  - [10] T. S. Sumanaweera. *Segmentation and distortion correction in medical imaging*. PhD thesis, Stanford University, 1992.
  - [11] D. Wang, W. Strugnell, G. Cowin, D.M. Doddrell, and R. Slaughter. Geometric distortion in clinical MRI systems Part I: evaluation using a 3D phantom. *Journal of Magnetic Resonance Imaging*, 22:1211–1221, 2004.
  - [12] D. Wang, W. Strugnell, G. Cowin, D.M. Doddrell, and R. Slaughter. Geometric

distortion in clinical MRI systems Part II: correction using a 3D phantom. *J. Magn. Reson. Imaging*, 22:1223–1232, 2004.

- [13] Robert Wilson. Radiological use of fast protons. *Radiology*, pages 487–491, 1946.